Confining Effective Theories Based on Instantons and Merons [*]

F. Lenz[a], J. W. Negele[b] and M. Thies[a]

[a] Institute for Theoretical Physics III
University of Erlangen-Nürnberg
Staudstrasse 7, 91058 Erlangen, Germany

[b] Center for Theoretical Physics,
Laboratory for Nuclear Science, and Department of Physics
Massachusetts Institute of Technology
Cambridge, Massachusetts 02139, U.S.A.

Abstract

An effective theory based on ensembles of either regular gauge instantons or merons is shown to produce confinement in SU(2) Yang-Mills theory. When the scale is set by the string tension, the action density, topological susceptibility and low-lying glueball spectrum are similar to those arising in lattice QCD. The physical mechanism producing confinement is explained, and a number of analytical insights into the effective theory are presented.

1 Introduction

Understanding the mechanism of confinement in quantum chromodynamics (QCD) is a fundamental but elusive challenge. Lattice calculations convincingly demonstrate that QCD yields confinement, but do not yet elucidate its mechanism. Although the strong coupling expansion produces an area law by disorder already in lowest order, this disorder alone is not the whole story as evidenced by the fact that the strong coupling expansion also erroneously yields confinement in U(1) gauge theory. Hence, in this work, we develop a confining effective theory based on degrees of freedom arising naturally from QCD. We explore in detail how confinement arises, and the degree to which this effective theory approximates the results of SU(2) lattice gauge theory.

There has been a long and fruitful history of seeking to understand nonperturbative QCD analytically by expanding the path integral for the partition function around stationary classical solutions and evaluating the fluctuations around these solutions. Central to this approach was the discovery of instantons [1] that satisfy the classical Euclidean Yang-Mills equations and implement the tunneling required between different winding number sectors of the Θ vacuum. Since instantons can be transformed to the singular gauge in which the gauge field falls off like $\sim 1/x^3$, a dilute gas of these instantons is an approximate solution to the field equations. The contribution of this dilute instanton gas to the potential between two static color charges can be calculated analytically, and was shown not to produce confinement [2]. Whereas an instanton that contributes to two opposite Wilson lines in a Wilson loop does contribute to a linear term to the potential, when the integral over color orientations of independent instantons that affect only one or the other Wilson line is performed, these uncorrelated contributions do not produce a linear term. Hence at separation larger than the instanton size, the potential becomes a constant and fails to confine.

When instantons failed to produce confinement, there was then hope that merons [3], solutions to the Yang-Mills equations with topological charge 1/2, would do so. Although a free meron has an action that diverges logarithmically with the volume, a pair of merons has a finite action that depends logarithmically on the separation. If the coupling is strong enough that the logarithmic potential is weaker than the entropy associated with the Euclidean separation ($\sim r^3 = \mathrm{e}^{3\ln r}$), meron pairs could dissociate and form a meron gas. Since meron fields only fall off as $\sim 1/x$, they are expected to be more effective in disordering than singular gauge instantons and thus potentially be a more effective mechanism for confinement [4, 5, 6]. Unfortunately the same $\sim 1/x$ behavior that makes them a candidate for confinement renders them intractable analytically, and as a result they have never been shown by analytic arguments to be responsible for confinement.

Motivated by the quark zero modes associated with instantons and the 't Hooft interaction governing light quarks, highly successful instanton liquid models, which had to be implemented numerically, were developed that provide clear insight into the role instantons play in chiral symmetry breaking and reproduce many of the salient features of QCD with light quarks [7, 8, 9, 10]. For our present purposes, it is best to think of an instanton liquid as an effective theory in which one parameterizes a set of gauge configurations in terms of the positions and color orientations of an ensemble of instantons to represent the salient degrees of freedom for gluons. Because the field equations are nonlinear, the superposition of a set of instanton

solutions is not a classical solution to the field equations. Hence, rather than summing over a set of classical solutions, one is approximating the original functional integral for the partition function over gauge fields by performing the integral over these effective degrees of freedom, for example by using the Metropolis algorithm to sample configurations. Physically, this sampling will favor the appropriate configurations that are energetically and entropically optimal. Because the gauge fields of singular gauge instantons fall off as $\sim 1/x^3$, a random instanton liquid in which the positions and color orientations of instantons are chosen randomly does not differ qualitatively from one generated by more sophisticated Metropolis sampling, so most of the qualitative phenomena occur in a random instanton liquid. As in the case of the dilute instanton gas, Wilson loops in a random instanton liquid also show no confinement at distances larger than the instanton size.

In the present work, we consider a more general class of effective theories based on ensembles of regular gauge instantons or merons, whose fields fall off like $\sim 1/x$, so that the resulting superposition of gauge fields is not close to a classical solution. Throughout this work, we will refer to regular gauge instantons or merons as *pseudoparticles*. The term *instanton* will always mean a regular gauge instanton, and if we wish to refer to a singular gauge instanton, we will always do so explicitly. Although it is analytically intractable to perform the resulting integral of the partition function over the pseudoparticle collective coordinates, it is straightforward to do so numerically using the Metropolis algorithm. Whereas most random choices of pseudoparticle fields create a large background field yielding an unphysically high action density, Metropolis sampling selects the particular configurations in which the collective coordinates are correlated in such a way as to produce very low action density. In this way, one can achieve the balance of energy and entropy in ensembles based on regular gauge pseudoparticles that is conceptually equivalent to what has been done in the past with singular gauge instantons.

This more general class of theories based on pseudoparticles combines both confinement and the successes of previous singular gauge instanton liquid models. As will be shown below, color correlations are required to superpose the long range pseudoparticle gauge fields to create the small background fields whose low action allows them to dominate the path integral. These also produce the correlations necessary to yield an area law for large Wilson loops and thus produce confinement. The short distance "spikes" in the gluon field arising from the short distance behavior of small merons or instantons behave just like the spikes in conventional singular gauge instanton liquid models, and thus produce the physics associated with the 't Hooft interaction and chiral symmetry breaking. Pseudoparticle ensembles were first used by the present authors to study meron ensembles [11], where there is no singular gauge alternative. However, in the context we have just described, it is clear that one should also consider regular gauge instantons. Indeed, since the gauge for each instanton is defined relative to its position, the fields obtained by superposing N singular gauge instantons is drastically different from the one obtained by transforming each of these instantons to the regular gauge and superposing the resulting fields. Neither is a classical solution of the Yang-Mills equations, and neither is preferred on physical grounds. Hence, in exploring the full physics based on classical solutions, it is essential to study both alternatives. Although we will not develop it further in this work, Ref. [11] discusses how one may expect center symmetry to be realized in pseudoparticle effective theories. A closely related effective theory [12] superposes pseudoparticle fields with dynamically determined amplitudes and generalizes to finite temperature, where a clear crossover in the Polyakov loop is observed from a nearly vanishing value at zero temperature to a magnitude close to unity at high

temperature.

The primary goals of this work are to understand the mechanism by which this effective theory produces confinement and other observed properties of SU(2) gauge theory, and explore its success and limitations in quantitatively approximating the results of lattice QCD calculations of the action density, topological susceptibility, and glueball masses. Although we will discuss both instanton and meron pseudoparticles in detail and give extensive examples for both, the primary focus in comparing with the lattice QCD spectrum is on the confining instanton theory. We will show that the confining instanton theory has essentially all the advantages of previous random and interacting singular gauge instanton models, with the added feature of incorporating confinement. To obtain insight into the effective pseudoparticle theory, we will strongly emphasize analytic arguments wherever possible, as indicated in the outline below.

The outline of this paper is as follows. Section 2 describes the details of the pseudoparticle ensembles and some relevant analytical properties. In particular, since one might be concerned that the long range fields of pseudoparticles are necessarily large, we present a simple example of how sets of merons can be chosen such that the leading order $1/x^4$ term in the action at large distances vanishes identically. Section 3 describes random and correlated pseudoparticle ensembles. For pedagogical purposes, we begin with an ensemble in which the pseudoparticle positions and color orientations are selected randomly without correlations. Although this ensemble has unphysical features, it enables us to make instructive analytical arguments. We then allow Metropolis dynamics to produce the appropriate color and spatial correlations. The resulting gauge fields are shown to have a proper thermodynamic limit and to be composed of small background fields plus "spikes" at the locations of pseudoparticles. By separately applying Metropolis dynamics to only color parameters and then both color and spatial parameters, we show that the dominant correlations are in the color degrees of freedom. Section 4 addresses Wilson loops and confinement. When scaled appropriately, Wilson loops are shown to lie on a universal scaling curve, which is nearly independent of the pseudoparticle size and the coupling constant and which shows a clear area law indicating confinement. The behavior of Wilson loops in both the small size and large size limits is explained analytically. We also show that the distribution of Wilson loops follows the diffusion behavior of Ref. [13] and that Wilson loops in higher representations exhibit Casimir scaling, both of which are in agreement with lattice QCD. Section 5 presents calculations of physical observables. Since the theory is confining, we can set the scale by the measured string tension and compare unambiguously with lattice calculations in which observables are also specified in terms of the measured string tension. The two most robust observables are the gluon condensate and the topological susceptibility, and both instanton and meron ensembles are shown to yield values in units of the string tension in qualitative agreement with lattice QCD. We show that for many operators of interest, the effective theory produces Euclidean correlation functions with the proper physical behavior. The correlation function of the topological charge density displays the proper negativity behavior, and operators constructed from field-strengths and Wilson loops enable us to measure the masses of 0^+, 1^-, 1^+, 2^+, and 2^- glueball states. Aside from an overall scale factor which we discuss, this glueball spectrum is in qualitative agreement with lattice QCD. The conclusions are summarized in the final Section 6.

2 Ensembles of Pseudoparticles

2.1 Pseudoparticle Properties and Definition of Pseudoparticle Ensembles

In this work, we explore the idea that pseudoparticles, i.e., merons or regular gauge instantons, are the essential degrees of freedom in SU(2) Yang-Mills gauge theory by writing the partition function as a path integral of an effective action depending on the positions and color orientations of an ensemble of pseudoparticles,

$$Z = \int dz_i dh_i e^{-\frac{1}{g^2} S[A(z_i, h_i)]} \,. \tag{1}$$

We identify the effective action S with the standard (Euclidean) action

$$S = \int_V d^4 x \, s(x), \quad s(x) = \frac{1}{4} F^a_{\mu\nu} F^a_{\mu\nu} \,, \tag{2}$$

associated with the fields in the space-time region V. Dual field-strength and topological charge density are defined by

$$\tilde{F}^a_{\mu\nu} = \frac{1}{2} \epsilon_{\mu\nu\sigma\rho} F^{a\,\sigma\rho} \,, \quad \tilde{s}(x) = \frac{1}{4} F^a_{\mu\nu} \tilde{F}^a_{\mu\nu} \,. \tag{3}$$

The gauge field for a pseudoparticle in Lorentz gauge with its center at the origin, after appropriate choice of the coordinate system in color space and after regularization of the singularity, is given by

$$a_\mu(x) = \xi \frac{\eta_{a\mu\nu} x_\nu}{x^2 + \rho^2} \frac{\sigma^a}{2} \,, \tag{4}$$

with $\xi = 1$ denoting merons and $\xi = 2$ instantons. Color and space-time dependence are correlated via the 't Hooft tensor

$$\eta_{a\mu\nu} = \epsilon_{a\mu\nu} + \delta_{a\mu}\delta_{\nu 0} - \delta_{a\nu}\delta_{\mu 0}.$$

For instantons and for merons of vanishing size ρ, $a_\mu(x)$ is a solution of the Euclidean classical field equations [1, 3]. The gauge fields of anti-merons or anti-instantons differ in sign if one of the space-time indices is 0. The field-strength of the pseudoparticles, its dual, the action density, the topological charge density and the topological charge are given by

$$F^a_{\mu\nu} = \frac{\xi}{(x^2 + \rho^2)^2} \left[-\eta_{a\mu\nu}((2-\xi)x^2 + 2\rho^2) + (2-\xi)(\eta_{a\mu\rho}x^\nu - \eta_{a\nu\rho}x^\mu)x^\rho \right] \,, \tag{5}$$

$$\tilde{F}^a_{\mu\nu} = \frac{\xi}{(x^2 + \rho^2)^2} \left[-2\rho^2 \eta_{a\mu\nu} - (2-\xi)(\eta_{a\mu\rho}x^\nu - \eta_{a\nu\rho}x^\mu)x^\rho \right] \,, \tag{6}$$

$$s_0(x) = \frac{3\xi^2}{2(x^2 + \rho^2)^4} \left[((2-\xi)x^2 + 2\rho^2)^2 + 4\rho^4 \right] \tag{7}$$

$$\tilde{s}_0(x) = \pm \frac{6\xi^2 \rho^2}{(x^2 + \rho^2)^4} \left[2\rho^2 + (2-\xi)x^2 \right] \,, \tag{8}$$

5

$$\nu = \frac{1}{8\pi^2} \int \mathrm{d}^4 x \, \tilde{s}_0(x) = \pm \frac{\xi}{2} . \tag{9}$$

Pseudoparticles and anti-pseudoparticles differ in the sign of the topological charge and its density. We note the difference in the asymptotic behavior of the field-strength of instantons and merons. The meron field-strength decays asymptotically as $1/x^2$, giving rise to an infrared logarithmic singularity in the action. For vanishing size, the action of a meron is also logarithmically divergent in the ultraviolet, so for merons, the size parameter ρ acts as an ultraviolet regulator.

An important quantity in our study of confinement will be the Wilson loop

$$W = \frac{1}{2} \operatorname{tr} \left\{ P \exp \mathrm{i} g \oint_{\mathcal{C}} A_\mu(x) \mathrm{d}x^\mu \right\} . \tag{10}$$

The integral in (10) is ordered along the closed path $\mathcal{C}$. Here we compile the relevant result for Wilson loops in the field of single pseudoparticles. Pseudoparticle fields [Eq. (4)] in a "spacelike" plane with $x_4 = 0$ are of the form

$$\mathbf{a} = \frac{\xi}{2} \frac{\mathbf{x} \times \boldsymbol{\sigma}}{\mathbf{x}^2 + \rho^2} .$$

Analytical expressions can be derived if the center of the pseudoparticle fields is in the plane of the Wilson loop. In this case, for a loop in the (x_1, x_2) plane,

$$a_1 = \frac{\xi}{2} \frac{x_2}{x_1^2 + x_2^2 + \rho^2} \sigma_3, \quad a_2 = -\frac{\xi}{2} \frac{x_1}{x_1^2 + x_2^2 + \rho^2} \sigma_3$$

and the field is abelian pointing in the 3 direction in color space. For calculation of the Wilson loop we can use Stokes' theorem with

$$(\operatorname{rot} \mathbf{a}^3)_3 = \frac{\xi}{2} \frac{\rho^2}{(x_1^2 + x_2^2 + \rho^2)^2}$$

and obtain for a circular Wilson loop (radius r) with the center of the circle and of the pseudoparticle coinciding

$$\oint a_\mu \, \mathrm{d}x^\mu = \int_\Sigma \mathrm{d}\boldsymbol{\sigma} \operatorname{rot} \mathbf{a} = \xi \pi \frac{r^2}{r^2 + \rho^2} \sigma_3.$$

In the limit of vanishing size,

$$\operatorname{rot} \mathbf{a}_3 = \xi \pi \, \delta^{(2)}(\mathbf{x}) \sigma_3, \quad \rho \to 0$$

and therefore the Wilson loop in a plane containing the singularity of the pseudoparticle field (position $\mathbf{x}$) becomes

$$W(\mathbf{x}) = (-1)^{\xi \theta(\mathbf{x})}, \quad \theta(\mathbf{x}) = 1 \, (0) \text{ if } \mathbf{x} \text{ is inside (outside) the loop.} \tag{11}$$

Instantons generate a trivial Wilson loop. This is true everywhere, not only if the center is located on the plane of the Wilson loop. For $\rho = 0$ the instanton field is a pure gauge,

$$A_\mu = \mathrm{i} \Omega_I \partial_\mu \Omega_I^\dagger \tag{12}$$

6

with

$$\Omega_I = \frac{x^4 + \mathrm{i}\boldsymbol{\sigma}\mathbf{x}}{x^2}, \tag{13}$$

and therefore loops not passing through the singularity generate

$$W_{\mathrm{Inst}} \equiv 1.$$

The Wilson loop of merons cannot be evaluated in closed form if the plane of the loop does not contain the singularity.

The ensembles to be considered in this study contain field configurations obtained by superposition of pseudoparticles and anti-pseudoparticles of fixed and equal number $N_P/2$,

$$A_\mu(x) = \sum_{i=1}^{N_P} h(i) a_\mu(x - z(i)) h^{-1}(i). \tag{14}$$

Such a configuration is specified by the position of the centers $z(i)$ and their color orientations

$$h(i) = h_0(i) + \mathrm{i}\mathbf{h}(i) \cdot \boldsymbol{\sigma}\,, \qquad h_0^2(i) + \mathbf{h}^2(i) = 1. \tag{15}$$

In the ensembles to be discussed, the location of the merons is restricted to a hypercube

$$-1 \leq z_\mu(i) \leq 1, \quad V = 16\,.$$

Our standard choice for the meron size and coupling constant is

$$\rho = 0.16\,, \quad g^2 = 32\,. \tag{16}$$

We will see later that after rescaling, our results have very little dependence on these values.

2.2 Finite Action Density of Pseudoparticles

The infrared divergence in the action of a meron may appear as an obstacle in their use as building blocks of field configurations with (infrared) finite action. A similar concern arises in the superposition of (regular gauge) instantons. However, here we show that with an appropriate choice of the color orientation, the action of a cluster of merons of finite size can be made finite. Similar arguments apply for clusters of regular gauge instantons.

By dimensional arguments, the leading term of the action density of a collection of merons behaves asymptotically as

$$s \sim S_{\mathrm{asy}} \frac{1}{x^4}$$

and therefore leads to a total action that is logarithmically divergent in the infrared. To calculate the coefficient S_{asy} we proceed by averaging over the orientation. Useful identities are:

$$\frac{1}{\Omega} \int \mathrm{d}\Omega\, \hat{x}_\mu \hat{x}_\nu \hat{x}_\rho \hat{x}_\sigma = \frac{1}{24} \Big[\delta_{\mu\rho}\delta_{\nu\sigma} + \delta_{\mu\sigma}\delta_{\nu\rho} + \delta_{\mu\nu}\delta_{\rho\sigma} \Big]\,,$$

7

$$\frac{1}{\Omega}\int d\Omega\,\hat{x}_\mu\hat{x}_\nu = \frac{1}{4}\delta_{\mu\nu}\,,\quad \frac{1}{\Omega}\int d\Omega\,(\hat{x}_\nu)^4 = \frac{1}{8}\,.$$

We introduce the notation

$$\eta(i)_{a\mu\nu} = \eta_{a\mu\nu}\quad \text{if } i\text{-th pseudoparticle is a meron}\,,$$
$$\eta(i)_{a\mu\nu} = \bar{\eta}_{a\mu\nu}\quad \text{if } i\text{-th pseudoparticle is an anti-meron}\,,$$

and find

$$\eta_{e\mu\rho}(i)\eta_{f\nu\rho}(j)\eta_{g\mu\nu}(k) = 4\delta_{ijk}\epsilon_{efg}\,,\quad \eta_{e\mu\rho}(i)\eta_{e'\mu\rho}(k)\eta_{f\nu\sigma}(j)\eta_{f'\nu\sigma}(l) = 16\delta_{ik}\delta_{jl}\delta_{ee'}\delta_{ff'}$$

$$\eta_{e\mu\rho}(i)\eta_{e'\mu\sigma}(k)\eta_{f\nu\sigma}(j)\eta_{f'\nu\rho}(l) = 4\Big[\delta_{ik}\delta_{jl}\delta_{ee'}\delta_{ff'} + \delta_{il}\delta_{jk}\delta_{ef'}\delta_{fe'} + (1-2\delta_{ijkl})\delta_{ij}\delta_{kl}\delta_{ef}\delta_{e'f'}\Big]\,,$$

$$\epsilon^{abc}\epsilon^{ab'c'}u^{be}(i)u^{b'e'}(k)u^{bcf}(i)u^{c'f'}(l) = \big(u^\dagger(i)u(k)\big)_{ee'}\big(u^\dagger(j)u(l)\big)_{ff'} - \big(u^\dagger(i)u(l)\big)_{ef'}\big(u^\dagger(j)u(k)\big)_{fe'}\,.$$

After a tedious calculation, we arrive at the following expression for the coefficient $S_{\rm asy}$:

$$S_{\rm asy} = 2\mathrm{tr}\,(V+\bar{V}) - 6\Big[\det U + \det\bar{U}\Big] - \frac{1}{4}\Big[\mathrm{tr}\,V^2 - (\mathrm{tr}\,V)^2 + \mathrm{tr}\,\bar{V}^2 - (\mathrm{tr}\,\bar{V})^2\Big] - \frac{1}{3}\Big[\mathrm{tr}\,V\bar{V} - \mathrm{tr}\,V\,\mathrm{tr}\,\bar{V}\Big]$$

(17)

with

$$U = \sum_{i\in M}u(i),\ \bar{U} = \sum_{i\in\bar{M}}u(i),\quad V = UU^\dagger,\quad \bar{V} = \bar{U}\bar{U}^\dagger.$$

(18)

The color orientation of 4 merons can be chosen such as to make the leading asymptotic contribution to the action vanish. This corresponds to a neutral object. From the trivial identity

$$0 = \begin{pmatrix} 1 & 0 & 0 \\ 0 & 1 & 0 \\ 0 & 0 & 1 \end{pmatrix} + \begin{pmatrix} 1 & 0 & 0 \\ 0 & -1 & 0 \\ 0 & 0 & -1 \end{pmatrix} + \begin{pmatrix} -1 & 0 & 0 \\ 0 & 1 & 0 \\ 0 & 0 & -1 \end{pmatrix} + \begin{pmatrix} -1 & 0 & 0 \\ 0 & -1 & 0 \\ 0 & 0 & 1 \end{pmatrix}$$

and by comparison with the representation of the color matrices u

$$u^{bc} = \delta_{bc}(h_0^2 - \mathbf{h}^2) + 2h_0 h_a \epsilon^{abc} + 2h_b h_c\,,$$

(19)

we read off that 4 merons with the color orientation of the i-th meron given by $h_i = 1$ yield a vanishing $1/x^4$ term in the asymptotic expansion of s. Such configurations exhibit confinement of their building blocks, analogous to the role of the gluons, since a complete dissociation of such a pseudoparticle cluster is accompanied by an infinite increase in the action.

The pseudoparticle ensembles have been generated by Monte Carlo sampling of the action in the path integral, Eq. (1). In each step of a Metropolis update, the position and color orientation of a given meron are tentatively changed, the induced changes in the action density are evaluated at a set of mesh points distributed over the whole volume, and the configuration is accepted or rejected based on the global change in action. The long range nature of the meron fields makes the changes extend throughout the whole system.

3 Stochastic and Correlated Pseudoparticle Ensembles

Our goal is to calculate vacuum expectation values of observables via the path integral over the collective coordinates of our effective theory with pseudoparticle degrees of freedom

$$\langle \mathcal{O} \rangle = \frac{1}{Z} \int \mathrm{d}z_i \mathrm{d}h_i \mathrm{e}^{-\frac{1}{g^2} S[A(z_i, h_i)]} \mathcal{O}[A(z_i, h_i)], \tag{20}$$

where Z is the partition function defined in Eq. (1). As discussed in the introduction, it is useful to proceed in steps. We begin with an ensemble in which the pseudoparticle positions and color orientations are selected according to a uniform distribution. This corresponds to the strong coupling limit, in which g^2 is infinite so that the action does not affect the weight of each configuration. It will be fruitful to think of the present effective theory in the context of corresponding lattice calculations, and this stochastic ensemble will be comparable to the strong coupling limit of lattice QCD. As in lattice QCD, various quantities can be computed analytically in the strong coupling limit. The comparison with the stochastic ensembles will be a cornerstone for understanding the significantly more complex structure of the dynamically correlated ensembles.

Dynamical correlations are included using the Metropolis algorithm to sample variables with a probability distribution given by the action. Thus, in the usual way, to calculate the path integral $\int \mathrm{d}x \mathrm{e}^{-S(x)} \mathcal{O}(x)$, we change x with a microreversible change Δx, calculate the corresponding change in action, ΔS, and accept the new value $x + \Delta x$ with probability $P = \min\left(1, \mathrm{e}^{-\Delta S}\right)$.

The crucial step beyond the stochastic ensemble is to include dynamical correlations in the pseudoparticle color orientations. Update of pseudoparticle positions is much less important, but will always be included unless we want to highlight the difference. Thus both the positions $z(i)$ and the parameters $h(i)$ specifying the color orientations of all the pseudoparticles are equilibrated using Metropolis updates. We will show that these dynamical color correlations make a qualitative change in the physical observables. In order to allow for a variable ultraviolet scale, we will also consider ensembles of pseudoparticles with a uniformly distributed pseudoparticle size ρ.

3.1 Action Density

In the stochastic ensemble, the action density can be evaluated analytically by assuming that the average over the color orientations satisfies

$$u^{ac}(i)u^{bc}(j) \approx \delta_{ij}\delta_{ab} \,.$$

This leads to the following expression:

$$4s \approx \sum_{i=1}^{N_P} \left[F_{\mu\nu}^a(i) \, F_{\mu\nu}^a(i) + \sum_{j\neq i} \left[\left(A_\mu^b(i) \, A_\mu^b(i)\right) \left(A_\nu^b(j) \, A_\nu^b(j)\right) - \left(A_\mu^b(i) \, A_\mu^b(i)\right) \left(A_\nu^c(j) \, A_\nu^c(j)\right) \right] \right].$$

Using standard identities for the 't Hooft symbol, we obtain, cf. Eq. (4)

$$g^2 \, A_\mu^a(i) \, A_\nu^a(i) = \frac{\xi^2}{[(x - z(i))^2 + \rho^2]^2} \left(\delta_{\mu\nu} \, (x - z(i))^2 - (x - z_\mu(i)) \, (x - z_\nu(i)) \right) ,$$

which in the center of the cube ($x = 0$) yields

$$g^2 \sum_{i=1}^{N_P} A_\mu^a(i) \, A_\nu^a(i) \approx \frac{3\xi^2}{4} \delta_{\mu\nu} \sum_{i=1}^{N_P} \frac{z(i)^2}{[z(i)^2 + \rho^2]^2} \,. \tag{21}$$

Furthermore, with the action density of a single meron or instanton, cf. Eq. (7),

$$F_{\mu\nu}^a(i) F_{\mu\nu}^a(i) = \frac{6\xi^2}{[(x - z(i))^2 + \rho^2]^4} \left[\left((2 - \xi)(x - z(i))^2 + 2\rho^2 \right)^2 + 4\rho^4 \right], \tag{22}$$

we derive for the action density of the gauge field generated by N_P pseudoparticles

$$
\begin{aligned}
g^2 s(x) &= \frac{3\xi^2}{2} \sum_{i=1}^{N_P} \left[\frac{1}{((z(i) - x)^2 + \rho^2)^4} \left[\left((2 - \xi)(z(i) - x)^2 + 2\rho^2 \right)^2 + 4\rho^4 \right] \right. \\
&\quad + \left. \frac{3\xi^2}{4} \sum_{j \neq i} \frac{(z(i) - x)^2}{((z(i) - x)^2 + \rho^2)^2} \frac{(z(j) - x)^2}{((z(j) - x)^2 + \rho^2)^2} \right].
\end{aligned} \tag{23}
$$

Performing the ensemble average we obtain for a system of N_M merons

$$g^2 \langle s(x = 0) \rangle = 4.5 \, N_M + 1.03 \, N_M(N_M - 1). \tag{24}$$

Fig. 1 shows the action density for the stochastic and for dynamically correlated ensembles. We observe a qualitatively different behavior of the action density as function of the position in the cube for stochastic and dynamically correlated ensembles. In agreement with the expression (23), the action density of the stochastic ensemble peaks in the center of the cube and decreases by a factor of 2 when approaching the surface of the cube. The dynamically correlated ensembles, on the other hand, are approximately constant for $|x_\mu| \leq 0.8$ and thus seem to respect translational symmetry. This central region is used for the evaluation of observables. The values of the action density of stochastic and dynamically correlated ensembles differ by two orders of magnitude. The value of the action density of the stochastic ensemble in the center of the cube,

$$g^2 \langle s(x = 0) \rangle = 2.6 \cdot 10^5,$$

is, within 1%, correctly predicted by Eq. (24).

The one-pseudoparticle contribution to the action density in (24) arising from the abelian part of the field-strength yields an intensive contribution to the action density in the thermodynamic limit, up to a logarithmic correction. In contrast, in the thermodynamic limit, assuming a finite density of pseudoparticles, the non-abelian contributions to the field-strength are dominant and give rise to an action density increasing linearly with the volume for sufficiently small ρ. Stochastic cancellations are not sufficient to achieve volume independence. For a cube of side-length $2L$ with $L \to \infty$, the action density of N_M merons at the center of the cube is

$$\langle s(x = 0) \rangle \approx 1.29 \, \frac{N_M^2}{g^2 L^4}. \tag{25}$$

In our calculation, all interference terms have disappeared and the same result applies for an arbitrary mixture of a total of N_M merons and anti-merons; furthermore, the same number of
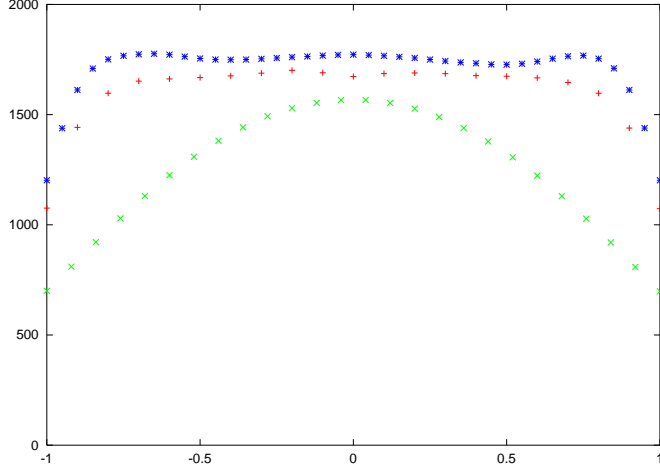
Figure 1: Action density $g^2\langle s(x)\rangle$ along the x-axis for the stochastic (rescaled) (green $\times$) and dynamically correlated ensembles with stochastic (blue $*$) and with dynamical positions (red $+$). Dynamical correlations decrease the value at the center of the cube from $261\,000$ to 1700.

regular instantons yields a 16 times larger action density. Clearly, the expression (25) is not compatible with a proper thermodynamic limit.

For comparison, we refer to the action density in the standard dilute instanton liquid. In this model the building blocks are instantons in singular gauge with the gauge field decreasing asymptotically like

$$A_\mu^a \sim \frac{1}{x^3}.$$

Thus for sufficiently low densities of instantons, $n_I \ll \rho^{-4}$, the action density is given by

$$g^2\langle s\rangle = 8\pi^2 n_I \tag{26}$$

and yields for N_I instantons in the volume 2^4

$$g^2\langle s\rangle \approx 4.94\,N_I. \tag{27}$$

The action associated with a field generated by stochastic superposition of 500 merons (regular instantons) is about 100 (16 000) times larger than the action of 500 singular instantons. As the expression (24) shows, the large value of the action density is not generated by pseudoparticles in the neighborhood, rather it results from the superposition of gauge fields with their $1/x$ asymptotic behavior generated by distant pseudoparticles. The contour plot of the action density of a single configuration of the stochastic meron ensemble (left side of Fig. 2) confirms this interpretation of the results. One clearly identifies a peak close to the center of the plane and the decrease towards the surface. No remnant of the building blocks, the merons, can be identified. The dynamical correlations change completely the picture (right side of Fig. 2). The weight determined by the action in Eq. (20) favors configurations where destructive interference between gauge fields of individual pseudoparticles prevent the formation of a large "mean field". In turn, the action density reflects clearly the structure of individual pseudoparticles. Screening of the gauge fields of the pseudoparticles is apparently also responsible for the restoration of translational symmetry. The comparison of the action density of merons and instantons in Fig. 3 demonstrates the similarity in the structure of the configurations generated by superimposing
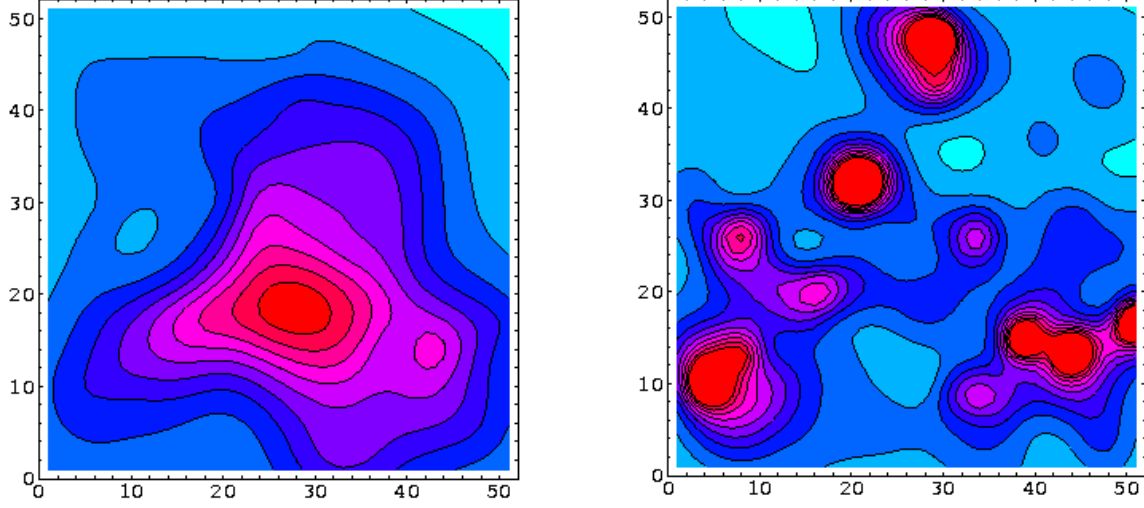
Figure 2: Contour plot of the action density in the (x, y) plane for a single configuration of the stochastic (left) and of the dynamically correlated meron ensemble (right) with $N_M = 500$. Left: $s[A] = 110000$, $15000 < s(x) < 327000$. Right: $s[A] = 1530$, $180 < s(x) < 11300$.

and dynamically correlating meron and instanton fields, respectively. The larger amplitudes of the instanton fields give rise to correspondingly larger values of the action density. These results suggest decomposing the action density of the dynamically correlated ensembles into a single instanton (s_I) or meron (s_M) and a background (s_B) component. For instantons with their finite value of the action, the simplest Ansatz for the action density is [cf. Eqs. (26,27)]

$$g^2 \langle s \rangle = g^2(s_I + s_B) = 8\pi^2 n_I + g^2 s_B = 4.94 \, N_I + g^2 s_B. \tag{28}$$

For the dynamically correlated instanton ensembles of Table 3 we find

$$\frac{s_B}{\langle s \rangle} = 0.55...0.65 \, . \tag{29}$$

The logarithmic infrared singularity of the meron action requires a slight modification in the Ansatz for the separation of single meron and mean-field contributions [11]. The single meron contribution is obtained by integrating $s(x)$ [Eq. (7)] over a sphere of radius r, which for small meron size ($\rho \ll r$) becomes

$$s_M = n \int^r \mathrm{d}^4 x s(x) \rightarrow 3\pi^2 n \left(\frac{5}{12} + \ln \frac{r}{\rho} \right). \tag{30}$$

The matching requirement on r,

$$s(r) = s_B,$$

yields the following expression for the action density,

$$\langle s \rangle = \left[s_B + n \frac{3\pi^2}{4} \left(\frac{5}{3} - \ln \frac{2}{3} s_B \rho^4 \right) \right]. \tag{31}$$

For the dynamically correlated meron ensembles of Table 2 we find

$$\frac{s_B}{\langle s \rangle} = 0.65...0.75 \, . \tag{32}$$
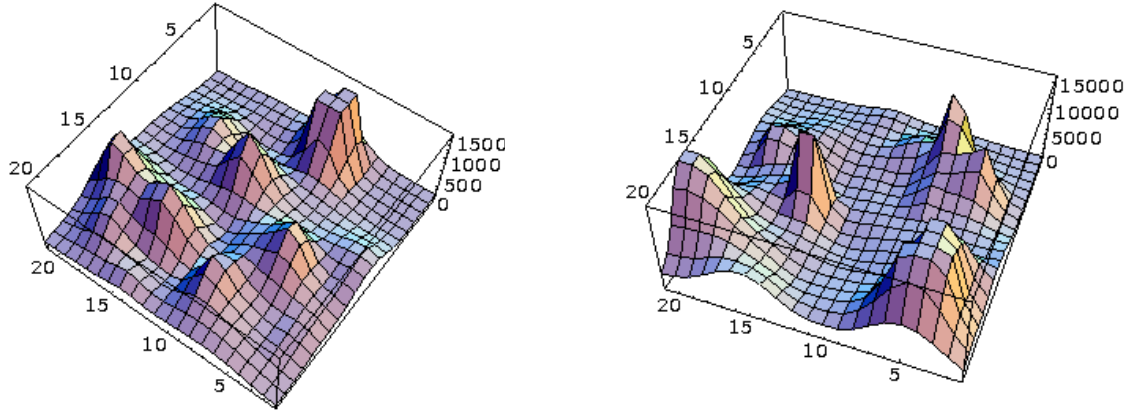
12

Figure 3: The action density in the (x, y) plane for a single configuration of 200 merons (left) and 200 regular instantons (right) respectively. Averaged over the plane the action density is 513 and 4700 respectively.

3.2 Wilson Loops

The following discussion focuses on the comparison of Wilson loops (10) in stochastic and dynamically correlated ensembles. A more thorough investigation of various issues concerning Wilson loops will be presented in later sections. Our standard choice for the path $\mathcal{C}$ in Eq. (10) is a rectangular path located in the (x_i, x_j) planes with the center at the origin and with the ratio of the sides equal to 2. Thus, for a given configuration, we evaluate 12 different Wilson loops W_{ij} and obtain our final results by taking the ensemble average and the average over the 12 different orientations,

$$\langle W \rangle = \frac{1}{12} \sum_{i \neq j} \langle W_{ij} \rangle. \tag{33}$$

The variance

$$\Delta W^2 = \frac{1}{12} \sum_{i \neq j} \Big(\langle W_{ij} \rangle - \langle W \rangle \Big)^2 \tag{34}$$

is used to estimate the statistical uncertainty in the determination of $\langle W \rangle$. Fig. 4 shows the Wilson loops for the stochastic and correlated ensembles as function of the area.

For sufficiently large loop size, we parameterize the logarithm of the Wilson loop as a sum of constant, perimeter ($\mathcal{P}$) and area ($\mathcal{A}$) terms,

$$\ln\langle W \rangle = \omega + \tau \mathcal{P} - \sigma \mathcal{A}, \tag{35}$$

with

$$\mathcal{A} = \frac{\mathcal{P}^2}{18}$$

for our standard choice of the path $\mathcal{C}$. The parameters of the fit are
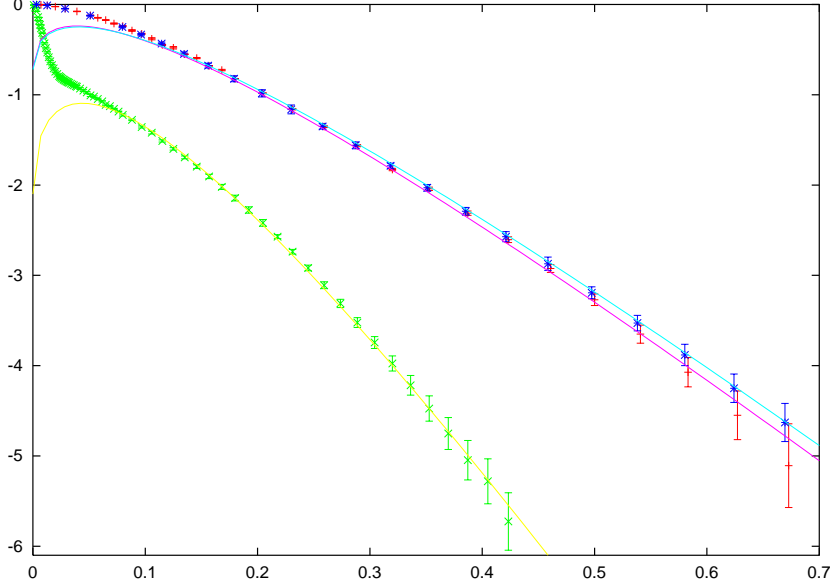
$$\omega = -2.1, \ \tau = 2.3, \ \sigma = 22.9 \tag{36}$$

13

Figure 4: Logarithm of a Wilson loop as a function of its area for three meron ensembles with $N_M = 500$: A stochastic ensemble (green ×), an ensemble with dynamical color orientations (pink −) and an ensemble with dynamical color orientations and dynamical meron positions (blue ∗). The fit curves are described in the text.

for the stochastic ensemble,

$$\omega = -0.7, \ \tau = 1.1, \ \sigma = 11.8 \tag{37}$$

for the ensemble with dynamical color orientations but random positions, and

$$\omega = -0.7, \ \tau = 1.1, \ \sigma = 11.5 \tag{38}$$

for the ensemble with dynamical color orientations and positions. As in the case of the action density, the change from the stochastic to the dynamically correlated ensemble is significant. In comparison, only minor changes result when, in addition, the meron positions are also dynamical variables. For $\mathcal{A} \geq 0.1$, the Wilson loops of the 3 ensembles are well reproduced by the parameterization (35). In particular, the results strongly suggest that all 3 ensembles give rise to an area law for sufficiently large size of the loops with a value of the string tension differing by a factor of 2 between stochastic and dynamically correlated ensembles. The large difference in the dimensionless ratios formed by action density and string tension,

$$\frac{g^2 s}{\sigma^2} \approx 500 \ \text{(stoch. ensemble)}, \quad \frac{g^2 s}{\sigma^2} \approx 11 \ \text{(dyn. corr. ensemble)}, \tag{39}$$

reflects the essential difference in the dynamics of the ensembles. It is plausible that this strong decrease in the dimensionless ratio arises from suppression of fluctuations. One expects that reducing the fluctuations has a larger effect on the positive definite local action density than on the non-local Wilson loop. As will be seen below, the large value of the action density expressed in units defined by the string tension rules out the stochastic ensemble as a viable model of the Yang-Mills dynamics.

Small Wilson Loops in the Stochastic Ensemble

In all the ensembles considered, the size dependence of small Wilson loops can be determined analytically. Since the configurations are built up by a finite number of pseudoparticles, fluctuations of the gauge fields cannot occur on arbitrarily small scales. In other words, for sufficiently small sizes, the gauge fields can be assumed to be spatially constant stochastic variables. For constant gauge fields, we use the identity

$$\mathrm{e}^{-\mathrm{i}\boldsymbol{\sigma}\mathbf{C}_2}\,\mathrm{e}^{-\mathrm{i}\boldsymbol{\sigma}\mathbf{C}_1}\,\mathrm{e}^{\mathrm{i}\boldsymbol{\sigma}\mathbf{C}_2}\,\mathrm{e}^{\mathrm{i}\boldsymbol{\sigma}\mathbf{C}_1} = 2\mathrm{i}\,\sin C_1\,\sin C_2\,e^{-\mathrm{i}\boldsymbol{\sigma}\mathbf{C}_2}\left(\hat{\mathbf{C}}_1 \times \hat{\mathbf{C}}_2\right)\boldsymbol{\sigma}\,\mathrm{e}^{\mathrm{i}\boldsymbol{\sigma}\mathbf{C}_2} \tag{40}$$

and obtain with

$$\mathbf{C}_i = \frac{1}{2}g\ell_i\mathbf{A}_i$$

$$W_0 = 1 - 2\sin^2\frac{1}{2}g\ell_1 A_1\,\sin^2\frac{1}{2}g\ell_2 A_2\left[1 - (\hat{\mathbf{A}}_1\hat{\mathbf{A}}_2)^2\right] = 1 - \frac{4}{3}\sin^2\frac{1}{2}g\ell_1 A_1\sin^2\frac{1}{2}g\ell_2 A_2. \tag{41}$$

In the last step we have averaged over the color orientations. The space-time independent gauge fields $\mathbf{A}_i$ are generated by a superposition of a large number of the stochastic variables (positions and color orientations) specifying the individual pseudoparticles. We therefore expect the space-time components $\mathbf{A}_i$ to be Gaussian distributed,

$$\rho(A_i)\mathrm{d}^3 A_i = \rho_0 A_i^2\mathrm{d}A_i\mathrm{d}\Omega_i\,\mathrm{e}^{-g^2 A_i^2/2\sigma_0^2}.$$

We determine the width of the distribution by the expectation value of $\mathbf{A}^2$ [cf. Eq. (21)]

$$\int\rho(A)g^2 A^2\mathrm{d}A\mathrm{d}\Omega = 3\sigma_0^2 = \frac{3\xi^2 N_P}{4}\,\langle\frac{x^2}{(x^2+\rho^2)^2}\rangle \tag{42}$$

and obtain

$$W_0 = 1 - \frac{1}{3}\left(1 - \left(1 - \ell_1^2\sigma_0^2\right)\mathrm{e}^{-\ell_1^2\sigma_0^2/2}\right)\left(1 - \left(1 - \ell_2^2\sigma_0^2\right)\mathrm{e}^{-\ell_2^2\sigma_0^2/2}\right), \tag{43}$$

with the values for the stochastic meron ensemble

$$\sigma_0^2 = 120 \quad\text{for}\quad N_P = N_M = 500\,, \quad \rho = 0.16\,. \tag{44}$$

The typical size of a gauge field component (with fixed color and space labels) is thus of the order of

$$gA_i^a \sim \frac{1}{2}\sqrt{N_M}\frac{1}{L} \approx 10\,.$$

Depending on N_P, to next order we still may consider x-dependent fluctuations to be small as compared to C_i but to be of the order of 1 and therefore not suppressed. We write

$$\tilde{\mathbf{C}}_i = \mathbf{C}_i + \boldsymbol{\gamma}_i \approx \mathbf{C}_i + \hat{\mathbf{C}}_i\gamma_i\,, \quad |\boldsymbol{\gamma}_i| \ll |\mathbf{C}_i|.$$

To leading order, the directions of $\tilde{\mathbf{C}}_i$ and $\mathbf{C}_i$ are identified but not their length. We find

$$\frac{1}{2}\mathrm{tr}\,\mathrm{e}^{-\mathrm{i}g\boldsymbol{\sigma}\tilde{\mathbf{C}}_2}\,\mathrm{e}^{-\mathrm{i}g\boldsymbol{\sigma}\tilde{\mathbf{C}}_1}\,\mathrm{e}^{\mathrm{i}g\boldsymbol{\sigma}\mathbf{C}_2}\,\mathrm{e}^{\mathrm{i}g\boldsymbol{\sigma}\mathbf{C}_1} \tag{45}$$

$$= \cos\gamma_1\cos\gamma_2 - \left(\hat{\mathbf{C}}_1\cdot\hat{\mathbf{C}}_2\right)\sin\gamma_1\sin\gamma_2 - 2\sin C_1\sin\tilde{C}_1\cdot\sin C_2\sin\tilde{C}_2\left(1 - (\hat{\mathbf{C}}_1\hat{\mathbf{C}}_2)^2\right).$$
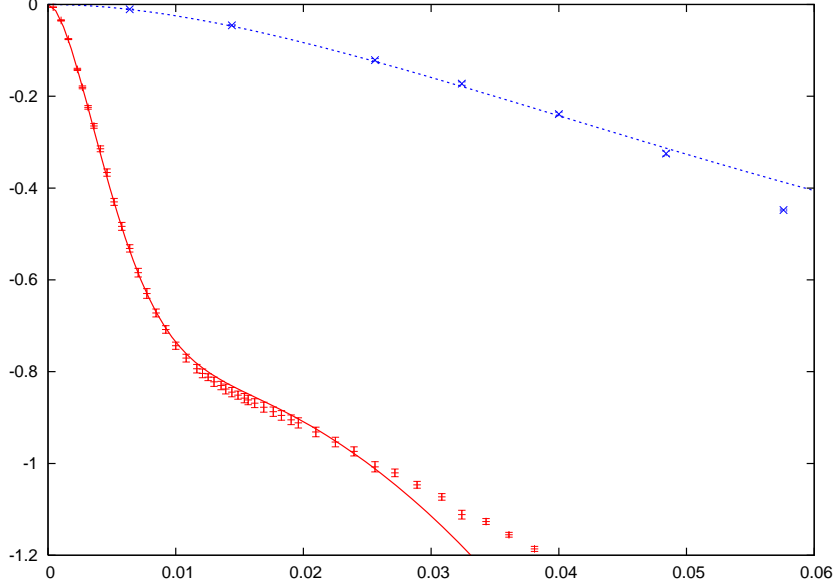
15

Figure 5: Enlarged portion of Fig. 4 for small size Wilson loops. The curves show the result of the small loop expansion [Eq. (46)] (red, lower curve) for the stochastic ensemble and the result [Eqs. (43,48)] (blue, upper curve) for the ensemble with dynamical meron positions and color orientations.

By Taylor expansion of the gauge fields at the center of the cube, the fluctuations can be calculated. With

$$A_\mu^a(x) = A_\mu^a(0) + \delta_\mu^a, \quad \gamma_\mu^a = \frac{1}{2}\ell_\mu\delta_\mu^a,$$

we obtain for the deviations along a rectangular loop in the $(1,2)$ plane

$$\sum_{a=1}^3 \gamma_\mu^{a\,2} = \xi^2(\ell_1\ell_2)^2 \sum_{i=1}^{N_P} \frac{3\,z(i)^4 + 4\,z(i)^2\rho^2 + 4\,\rho^4}{16\left(z(i)^2 + \rho^2\right)^4} \quad \mu = 1,2\,.$$

Treating the deviations as independent stochastic variables with a Gaussian distribution

$$\tilde{\rho}(\gamma) = \tilde{\rho}_0 e^{-\gamma_\mu^{a\,2}/\sigma_1^2}$$

of variance

$$\sigma_1^2 = \frac{1}{(\ell_1\ell_2)^2}\frac{2}{3}\sum_a \gamma_\mu^{a\,2}$$

we obtain

$$\langle\cos\frac{\gamma_1}{2}\rangle = \langle\cos\frac{\gamma_2}{2}\rangle = e^{-\sigma_1^2(\ell_1\ell_2)^2/4}.$$

In this approximation, the expectation value of the Wilson loop [Eq. (43)] acquires the following correction [cf. Eq. (45)],

$$W_1 = W_0 - 1 + e^{-\sigma_1^2(\ell_1\ell_2)^2/2}, \tag{46}$$

and we find for the stochastic meron ensemble

$$\sigma_1^2 = 118 \quad \text{for} \quad N_M = 500\,, \quad \rho = 0.16\,. \tag{47}$$

16

The agreement with the results of the numerical evaluation (cf. Fig. 5) confirms the role of the constant gauge fields for small size Wilson loops. The above analysis of the small Wilson loops applies to some extent also to the dynamical ensembles where spatial variations of the gauge fields cannot happen either on arbitrarily small scales. Assuming independence of the fluctuation of the constant gauge fields, we still may use the expression (43) and, in the absence of a closed expression for the fluctuations of the gauge fields, determine the value of the width

$$\sigma_0^2 = 10 \tag{48}$$

by a fit to our numerical results (cf. Fig. 5). The reduction in σ_0, i.e., in the size of the gauge field fluctuations, by one order of magnitude from the value (44) of the stochastic ensemble by the dynamics of the pseudoparticles is compatible with the reduction in the action density (dominated by the A^4 term), cf. Fig. 1.

3.3 Thermodynamic Limit

Unlike the stochastic ensemble, the dynamically correlated ensembles exhibit with the restoration of translational invariance a proper thermodynamic limit. In the case of stochastic ensembles, when doubling the linear dimensions of the system L with the density of pseudoparticles kept fixed, intensive quantities like the action density calculated in the stochastic ensemble do not remain invariant. The action density actually increases in this case by a factor 16 [cf. Eq. (25)]. Results for the dynamically correlated ensembles indicate significant improvement.
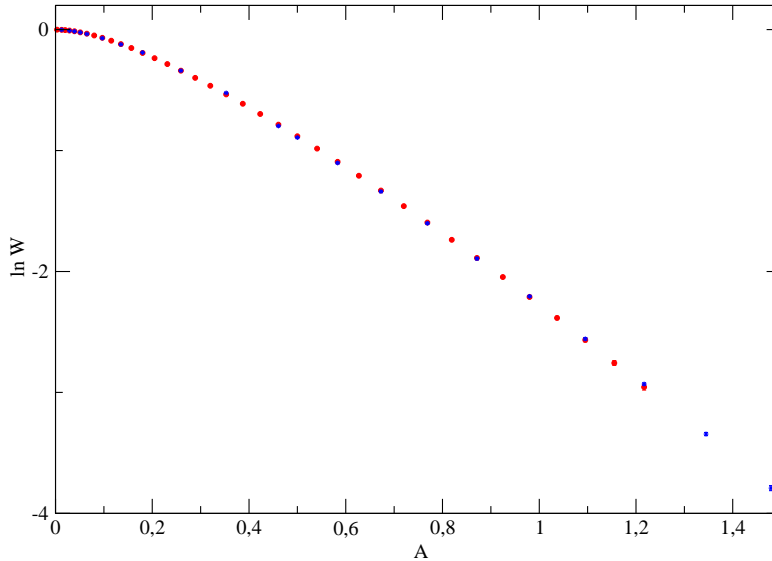

Figure 6: Logarithm of Wilson loop as function of the area for meron ensembles $N_M = 50$ ($L = 2$) (circle) and $N_M = 800$ ($L = 4$) (star).

The realization of translational symmetry (cf. Fig. 1), or the scaling properties to be discussed in

the next section, would be hard to understand without a proper behavior in the thermodynamic limit. Here we present the results of a direct numerical examination of the thermodynamic limit by doubling the side length L and increasing the number of merons from 50 to 800. To achieve

N_M	ρ	$\langle s \rangle$	$\chi^{1/4}$	$C_s(0)$	$C_{\tilde{s}}(0)$
50	0.16	273	0.66	$2.50 \cdot 10^5$	$1.86 \cdot 10^5$
800 ($L=4$)	0.16	284	0.66	$2.53 \cdot 10^5$	$1.88 \cdot 10^5$

Table 1: Test of thermodynamic limit for the vacuum expectation values of the action density s defined in (2) and of the topological susceptibility χ (95), and of the values of the correlation function of the action density (88) and the topological charge density (89) at zero separation.

high accuracy in this important test, we have generated ensembles which in comparison with our "standard" ensembles contain 4 times as many field configurations and where the action density in the update process has been evaluated at 3 times more meshpoints. The results in Fig. 6 and Table 1 demonstrate the agreement in the Wilson loops and in various other observables for these two ensembles. It is remarkable that the thermodynamic limit is established as a consequence of the dynamics of the pseudoparticles.

4   Wilson Loops in Correlated Pseudoparticle Ensembles

This section contains our main results concerning Wilson loops, an analysis of the structure of small Wilson loops and a discussion of the relation of our results to the general properties of Yang-Mills Wilson loops in the small and large loop limit as known from lattice gauge studies. The results have been obtained on the basis of about 150 000 - 250 000 configurations in each of the ensembles discussed in this section.

4.1   Scaling Properties

The Wilson loops evaluated in the meron and instanton ensembles with a wide range of pseudoparticle numbers exhibit a universal behavior as demonstrated by Figs. 7 and 8. After rescaling the area $\mathcal{A} \to \lambda \mathcal{A}$, the values of the Wilson loop lie on a universal scaling curve, where deviations from scaling are within the statistical uncertainties. To account for the rescaling of the area, we generalize the Ansatz (35) for the logarithm of the Wilson loop,

$$\ln\langle W \rangle = \omega + \tau \sqrt{\lambda}\, \mathcal{P} - \sigma \lambda \mathcal{A} \,. \tag{49}$$

For merons, the values of the universal parameters are

$$\omega = -0.95, \quad \tau = 1.34, \quad \sigma = 12.7 \,. \tag{50}$$

A central result of this work is that for both merons and instantons, for sufficiently large size, the logarithm of the Wilson loop decreases linearly with increasing area. This area law clearly demonstrates confinement in these pseudoparticle ensembles. The physical scale for each of
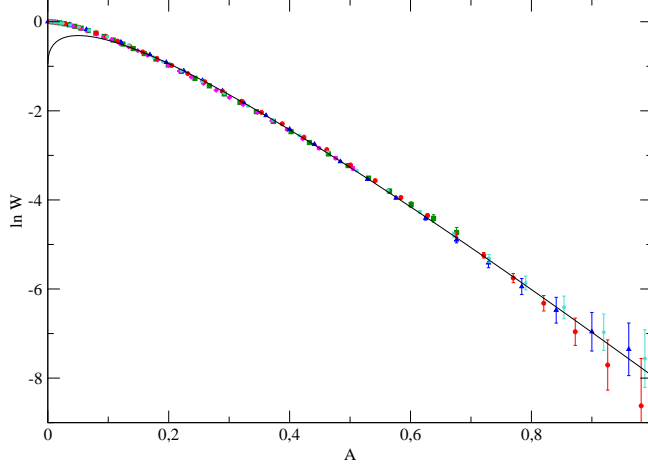
Figure 7: Logarithm of a Wilson loop as a function of its area for meron ensembles $N_M = 800$ ($L = 4$) (star), 100 (diamond), 200 (square), 500 (circle), 1000 (triangle). The values of the scale parameter λ are given in Table 2. Also shown is the curve corresponding to the parameterization (49) with the values of the parameters given in (50).

the pseudoparticle ensembles is obtained by identifying the value of $\lambda\sigma$ with the the value 4.4 fm^{-2}, i.e., the unit of length (u.l.) for each of the ensembles is determined by λ. For merons,

$$1\,\text{u.l.} = 1.70\sqrt{\lambda}\,\text{fm}\,. \tag{51}$$

The corresponding parameters for the instanton ensembles are

$$\omega = -0.52, \quad \tau = 1.18, \quad \sigma = 19.0, \quad 1\,\text{u.l.} = 2.08\sqrt{\lambda}\,\text{fm}\,. \tag{52}$$

Fig. 9 displays the dependence of our results on the pseudoparticle size and coupling constant. Whereas changes in the Wilson loops induced by changes in the pseudoparticle size ρ can be accounted for to a large extent by a change in the physical scale, variations in the coupling constant by a factor of 4 modify the shape beyond changes in the scale, and a tendency is visible for a slightly smaller string tension in the ensembles with variable pseudoparticle size. We note that in the update process for the ensembles with variable size, the sizes of the pseudoparticles are kept fixed. On the basis of the identification of the value of the string tension extracted from the Wilson loops with the empirical value, we can compare our results for various observables with those obtained in other approaches, in particular with lattice gauge results. The values of the scaling parameter λ together with other properties of meron and instanton ensembles are given in Tables 2 and 3. This first discussion of physical observables focuses on the action density and the topological susceptibility. Note that we refer in Tables 2 and 3 to results that will be explained in detail in section 5. From lattice SU(2) calculations for the action density the value $\langle s \rangle / \sigma^2 = 4.5$ [14] has been deduced. QCD sum rule results [15, 16] range from $\langle s \rangle / \sigma^2 = 4.5$ to 10. The necessity of subtracting divergent terms to define the continuum limit makes the uncertainty of these values of the action density, or equivalently of the gluon condensate, hard to assess. For instance, in the lattice calculations of Ref. [14], the divergent contributions are about a factor of 20-500 larger than the extracted value of $\langle s \rangle$. As discussed above, the pseudoparticle action density also contains contributions which in the limit of vanishing pseudoparticle size
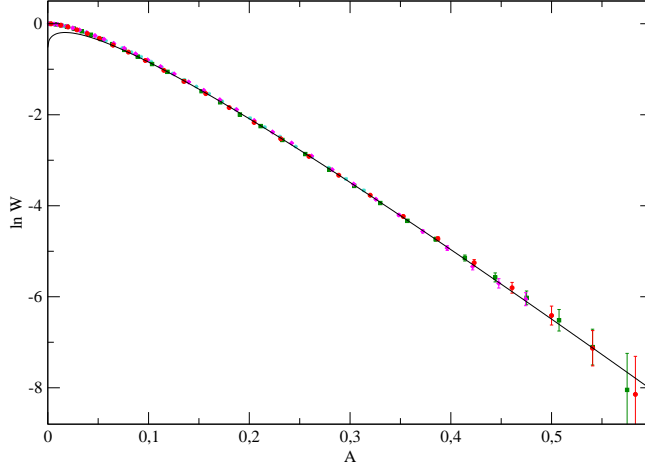
Figure 8: Logarithm of a Wilson loop as a function of its area for instanton ensembles $N_I = 50$ (star), 100 (diamond), 200 (square), 500 (circle). The area has been rescaled with λ given in Table 3. Also shown is the curve corresponding to the parameterization (49) with the values of the parameters given in (52).

$\rho \to 0$ become singular and should therefore be subtracted. Thus a more relevant quantity to be compared with the lattice and sum rule results is the "mean-field value" of the action density [cf. Eqs. (29,32)]. We find

$$\frac{s_B}{\sigma^2} \approx 8\ (10) \quad \text{for merons (instantons)}. \tag{53}$$

This discussion also shows that the presence of undamped fluctuations in the field configurations of the stochastic ensemble [cf. Eq. (39)] is in severe conflict with the lattice and sum rule results. The topological susceptibility is directly related to the η' mass by the Veneziano-Witten formula [17, 18] and is well measured in lattice QCD. From the results in Tables 2 and 3 we conclude

$$\chi^{1/4}/\sigma^{1/2} \approx 0.31\,, \quad \xi = 1\,; \quad 0.42 \leq \chi^{1/4}/\sigma^{1/2} \leq 0.48\,, \quad \xi = 2\,.$$

Both the meron and the instanton ensembles yield values of the susceptibility of the correct order of magnitude. The value for the instanton ensembles agrees within its 7% error bars with the SU(2) lattice result [19] $\chi^{1/4}/\sigma^{1/2} \sim 0.48$.

4.2   Small Size Wilson Loops and the U(1) Limit

Fields generated by superposition of a finite number of pseudoparticles are finite. Fluctuations do not occur with arbitrarily small wavelength. They are effectively cut off at length scales of the order of the pseudoparticle size or the average distance between neighboring pseudoparticles. As a consequence, the values of Wilson loops calculated in pseudoparticle ensembles vanish
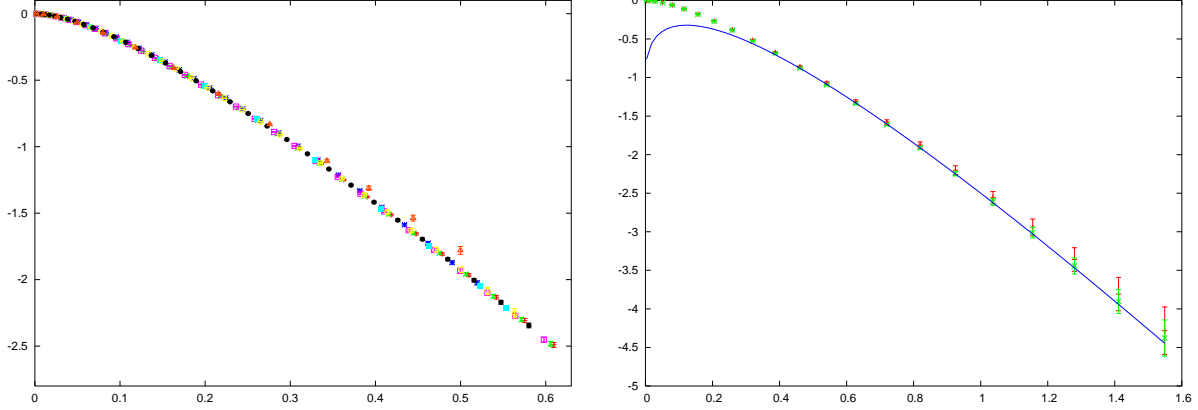
20

Figure 9: Logarithm of a Wilson loop as a function of its area for meron ensembles $N_M = 50$. Left : Ensembles with different values of the meron size ($0.01 \leq \rho \leq 0.16$) and of the coupling constant ($g^2 = 8, 32$). The area has been rescaled with values of λ in the range $0.31 \leq \lambda \leq 0.44$. Right: Ensembles of variable size uniformly distributed in the interval $0.03 \leq \rho \leq 0.17$ (red) and of fixed size $\rho = 0.10$ (green).

N_M	$\langle s \rangle$	λ	$\chi^{1/4}$	$C_s(0)$	$C_{\tilde{s}}(0)$	n_M	ρ	$\langle s \rangle$	$\chi^{1/4}$
-	-	-	-	-	-	[fm^{-4}]	[fm^{-1}]	[fm^{-4}]	[MeV]
1000	2742	1.25	1.19	$3.67 \cdot 10^6$	$2.49 \cdot 10^6$	4.8	0.30	210	118
500	1744	1.	1.01	$2.12 \cdot 10^6$	$1.45 \cdot 10^6$	3.8	0.27	209	120
200	897	0.69	0.9	$9.7 \cdot 10^5$	$7.0 \cdot 10^5$	3.2	0.23	226	124
100	507	0.52	0.77	$4.8 \cdot 10^5$	$3.6 \cdot 10^5$	2.8	0.20	225	124
50	249	0.37	0.66	$2.23 \cdot 10^5$	$1.78 \cdot 10^5$	2.7	0.16	218	132

Table 2: Properties of meron ensembles: Vacuum expectation values of the action density s defined in (2) and of the the topological susceptibility χ (95) (also in physical units), values of the scaling parameter λ (49), and values of the correlation functions of the action density (88) and the topological charge density (89) at zero separation with the standard choice of the parameters (16) for ensembles of N_M merons and with meron density $n_M = N_M/L^4$.

with vanishing loop size. This presence of an intrinsic cutoff prohibits a straightforward comparison of Wilson loops of pseudoparticle ensembles with field theoretic treatments in which for small sizes, Wilson loops approach the limit of the Maxwell theory and yield Coulomb-like static quark-antiquark potentials that diverge with decreasing distance of the sources. Although both stochastic and dynamically correlated ensembles suffer from this deficiency, the stochastic ensemble with its much larger fluctuations appears to exhibit a Coulomb like behavior for areas $\mathcal{A} \leq 0.01$ (cf. Figs. 4 and 5) and only for values $\mathcal{A} \leq 0.002$, does the Wilson loop show the quadratic dependence on the area. In the dynamically correlated ensembles we cannot identify such an intermediate Coulomb-like regime. For a meaningful interpretation we therefore have to account for the presence of this intrinsic ultraviolet cutoff and we will compare with Wilson loops in Maxwell theory in which the necessary ultraviolet regulator is kept finite.

For small loop size we expand the exponential in the definition of the Wilson loop in SU(2)

N_I	$\langle s \rangle$	λ	$\chi^{1/4}$	$C_s(0)$	$C_{\tilde{s}}(0)$	n_I	ρ	$\langle s \rangle$	$\chi^{1/4}$
-	-	-	-	-	-	[fm^{-4}]	[fm^{-1}]	[fm^{-4}]	[MeV]
500	5430	1.0	1.81	$2.7 \cdot 10^7$	$1.6 \cdot 10^7$	1.68	0.33	291	162
200	2490	0.66	1.49	$9.7 \cdot 10^6$	$6.6 \cdot 10^6$	1.54	0.27	307	164
100	1350	0.48	1.37	$5.1 \cdot 10^6$	$3.8 \cdot 10^6$	1.45	0.23	314	180
50	651	0.32	1.15	$2.3 \cdot 10^6$	$1.9 \cdot 10^6$	1.64	0.19	340	190

Table 3: Properties of instanton ensembles, as defined in Table 2.

Yang-Mills theory

$$W = \frac{1}{2}\,\mathrm{tr}\left\{ P \exp \mathrm{i}g \oint_{\mathcal{C}} A_\mu(x)\mathrm{d}x^\mu \right\} \approx 1 - \frac{3g^2}{8} \oint_{\mathcal{C}} \tilde{A}_\mu(x)\mathrm{d}x^\mu \oint_{\mathcal{C}} \tilde{A}_\mu(y)\mathrm{d}y^\mu. \tag{54}$$

Here, $\tilde{A}$ denotes one of the color components of the gauge field. For small loop size we compute the vacuum expectation value of the Wilson loop by identifying $\tilde{A}$ with an abelian gauge field and find

$$\langle W \rangle \approx 1 - \frac{3g^2}{8} \int J_{c\nu}(x) K(x-y) J_c^\nu(y)\mathrm{d}^4 x\,\mathrm{d}^4 y, \tag{55}$$

where

$$J_c^\mu(x) = \int \delta^4(x - x_c(s))\,\frac{\mathrm{d}x^\mu}{\mathrm{d}s}\,\mathrm{d}s$$

is the current of a charge transported along the curve $\mathcal{C}$. The Euclidean gauge field propagator K in Lorentz gauge is given by the inverse of the 4-dimensional Laplacian. The integral (55) requires regularization. We choose a heat kernel regularization and obtain for the regularized propagator in Maxwell theory

$$K(x) = \int \frac{\mathrm{d}^4 k}{(2\pi)^4}\,\mathrm{e}^{-\alpha k}\,\frac{\mathrm{e}^{ikx}}{k^2} = \frac{1}{4\pi^2 x^2}\left[1 - \frac{\alpha}{\sqrt{\alpha^2 + x^2}} \right]. \tag{56}$$

We consider rectangular loops with side lengths R and T and denote with

$$\omega(R,T) = \int_0^T \mathrm{d}x_0 \int_0^T \mathrm{d}y_0\, K\left(\sqrt{(x^0 - y^0)^2 + R^2}\right) \tag{57}$$

the contribution to W of the time-components of the two currents on opposite sides of the rectangle in the expression (55). The Wilson loop is obtained from the 4 contributions of time and space components on the same and on opposite sides of the rectangle,

$$\langle W \rangle \approx 1 - \frac{3g^2}{8}\left[\, \omega(0,T) + \omega(0,R) - \omega(R,T) - \omega(T,R)\,\right]. \tag{58}$$

The integral (57) can be evaluated in closed form with the result

$$\omega(R,T) = -\frac{1}{2\pi^2}\left[\, \ln \frac{\alpha + \sqrt{\alpha^2 + R^2 + T^2}}{\alpha + \sqrt{\alpha^2 + R^2}} - \frac{T}{R}\arctan T R\,\frac{\sqrt{R^2 + T^2 + \alpha^2} - \alpha}{R^2\sqrt{R^2 + T^2 + \alpha^2} + \alpha T^2}\,\right]. \tag{59}$$

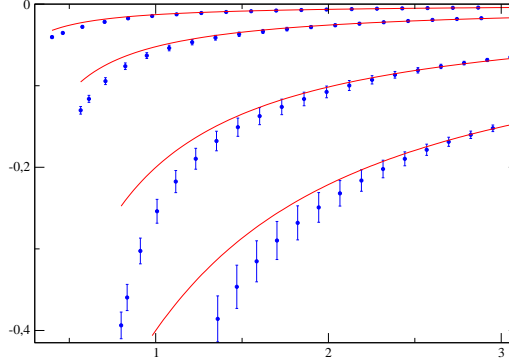Performing the limit $\alpha \to 0$, we obtain for $R \ll T$

Figure 10: Logarithm of rectangular Wilson loops of fixed area ($\mathcal{A} = 0.01, 0.02, 0.04, 0.06$) as a function of the perimeter for an ensemble with 500 instantons of variable size $\rho \leq 0.1$. The curves are obtained from Eqs. (58, 59) with the value (62) of the regulator.

$$\langle W \rangle \approx 1 + \frac{3g^2}{16\pi^2}\left[\frac{\pi T}{2R} + 1 - \frac{R+T}{\alpha} + 2\ln\frac{R}{2\alpha}\right], \tag{60}$$

which contains both the Coulomb potential and the self-energy of the static charges. On the other hand, in the limit of small loops and for fixed α, $\langle W \rangle - 1$ tends to zero with the square of the area

$$\langle W \rangle \approx 1 - \frac{g^2}{2}\left(\frac{3RT}{8\pi\alpha^2}\right)^2, \tag{61}$$

as is the case for Wilson loops in pseudoparticle ensembles. The small Wilson loops in the stochastic ensemble in Fig. 5 display these two different limits. The regime (61) of vanishing loop size is restricted to values of the area of the order of 10^{-3} and is followed by the Coulomb-like behavior associated with the limit (60) of vanishing regulator size, which extends up to values of the area of the order 10^{-2}. With the reduction in the fluctuations, the dynamically correlated ensembles do not explicitly show the Coulomb-like behavior. Nevertheless on the basis of this analysis we can understand the small loop limit of the dynamically correlated ensembles and make the connection to the perturbative U(1) limit.

For the comparison of the pseudoparticle Wilson loops with Wilson loops of the Maxwell theory (58,59) at finite α, we have determined the value of the regulator by a fit of expression (58) to the Wilson loops in the pseudoparticle ensembles. The results are shown in Fig. 10. The value of the regulator is

$$\alpha = 0.15. \tag{62}$$

The heat kernel regulated expression for the Wilson loop (58) reproduces the trend of the numerical results. Quantitative agreement is obtained for large values of the perimeter, i.e., for $R \ll T$.

4.3 Large Size Wilson Loops and the String Limit

Results from lattice gauge theories (cf. e.g. [20]) support the conjecture that large Wilson loops can be described by a an effective string theory. In the string picture, one assumes the Wilson

loop is determined by the string partition function [21]

$$W(R,T) = \int d[x_\perp] e^{-\sigma_{cl} RT - S_{qf}(x_\perp)}, \quad S_{qf} = \int_0^R \int_0^T d\xi_1 \, d\xi_2 \, \partial_\alpha x_\perp^\mu \, \partial_\alpha x_\perp^\mu . \tag{63}$$

Apart from the classical string energy σR, this expression accounts for the small quantum fluctuations around the classical string. The integral over the fluctuating transverse string coordinates $x^\mu(\xi_1, \xi_2)$ is given by the determinant of the two-dimensional Laplacian,

$$e^{-FT} = \int d[x_\perp] e^{-S_{qf}(x_\perp)} = \frac{1}{\det(-\Delta)} . \tag{64}$$

For computation of $\det(-\Delta)$, one imposes Dirichlet boundary conditions along the boundary of the Wilson loop. In terms of the resulting spectrum, the free energy F for a rectangular loop of side lengths R, T reads

$$FT = \sum_{m,n=1}^{\infty} \ln \left(\frac{\pi^2 m^2}{T^2} + \frac{\pi^2 n^2}{R^2} \right) . \tag{65}$$

In ζ function regularization [22], the following finite expression

$$\det(-\Delta) = \frac{1}{\sqrt{2R}} \eta\left(i\frac{T}{R}\right) \tag{66}$$

in terms of the Dedekind η function

$$\eta(z) = e^{i\pi z/12} \prod_{n=1}^{\infty} (1 - e^{2i\pi nz})$$

is obtained. The prefactor in the η function yields the well known Lüscher term [20], $\pi T/12R$, which dominates the logarithm of the Wilson loop in the limit of large T/R.

For the purpose of analyzing the Wilson loops in pseudoparticle ensembles, we need a regularization scheme that makes explicit the role of the cutoff. In heat kernel regularization, the expression for the free energy reads

$$TF(\lambda) = \sum_{m,n=1}^{\infty} \ln \left(\frac{\pi^2 m^2}{T^2} + \frac{\pi^2 n^2}{R^2} \right) e^{-\lambda \sqrt{\frac{\pi^2 m^2}{T^2} + \frac{\pi^2 n^2}{R^2}}} . \tag{67}$$

The leading term in λ^{-1} can be evaluated in closed form

$$\begin{aligned}
TF(\lambda) &\approx \frac{TR}{\pi^2} \int dp \, dq \, \ln(p^2 + q^2) \, e^{-\lambda \sqrt{p^2+q^2}} \\
&\approx \frac{4TR}{\pi} \left(-\frac{d}{d\lambda} \right) \int_0^\infty dp \, e^{-\lambda p} \ln p = \frac{4TR}{\pi} \frac{1}{\lambda^2} \left(\mathbf{C} - 1 - \ln \lambda \right) .
\end{aligned}$$

In the limit $\lambda \to 0$, a quadratically divergent correction to the string tension is obtained. As follows from dimensional arguments, the subleading linearly divergent (up to logarithms) terms are multiplying R and T.

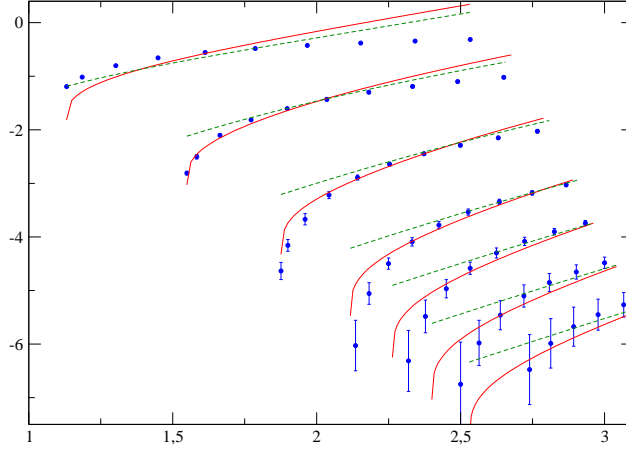For comparison with the large Wilson loops evaluated in the pseudoparticle ensembles, we

Figure 11: Logarithm of rectangular Wilson loops of fixed area $\mathcal{A}$ as a function of the perimeter for an ensemble with 500 instantons of variable size $\rho \leq 0.1$. The 7 values of the area vary between 0.08 and 0.40. The solid and dashed curves are obtained from Eqs. (70) and (68) with the values of the parameters given in Eqs. (71) and (69) respectively.

keep λ finite and introduce counterterms associated with the divergent contributions. We fit our numerical results for the Wilson loop with the Ansatz

$$\ln W = -TF(\lambda) + a + b(T + R) + \sigma_0 RT\,, \tag{68}$$

with the counterterms a, b and σ_0 depending on λ. We have applied this procedure to Wilson loops of ensembles with 500 instantons and merons respectively with variable size ($\rho \leq 0.1$). The fit to the pseudoparticle results yields the following values of the parameters,

$$\lambda = 0.25,\ a = -0.7,\ b = 1.8,\ \sigma_0 = -14\,. \tag{69}$$

As Fig. 11 shows, the string model defined by Eqs. (68,69) leads essentially to a linear dependence of the logarithm of the Wilson loops as a function of the perimeter with a very mild dependence of the slope on the value of the area. For sufficiently large aspect ratios of the loops, the string model reproduces the numerical results for the pseudoparticle ensembles. However the model misses the change in slope close to the threshold, i.e., in the limiting case of a square. For fixed area $\mathcal{A}$, the slope of the Wilson loop as a function of the perimeter $\mathcal{P}$ becomes in general infinite if the Wilson loop depends on $|T - R|$. We find

$$\frac{\partial}{\partial \mathcal{P}}|T - R|^\mu = \frac{\mu}{4}|T - R|^{\mu-2}\mathcal{P}\,,$$

i.e., a divergent slope at threshold is obtained for $\mu < 2$. The presence of such a term is indicated by the rapid change of the numerical results with $\mathcal{P}$ at the threshold $\mathcal{P} = 4\sqrt{\mathcal{A}}$. To account for this structure, we modify minimally our Ansatz (68),

$$\ln W = -TF(\lambda) + a + b\sqrt{T^2 - R^2} + \sigma_0 RT, \tag{70}$$
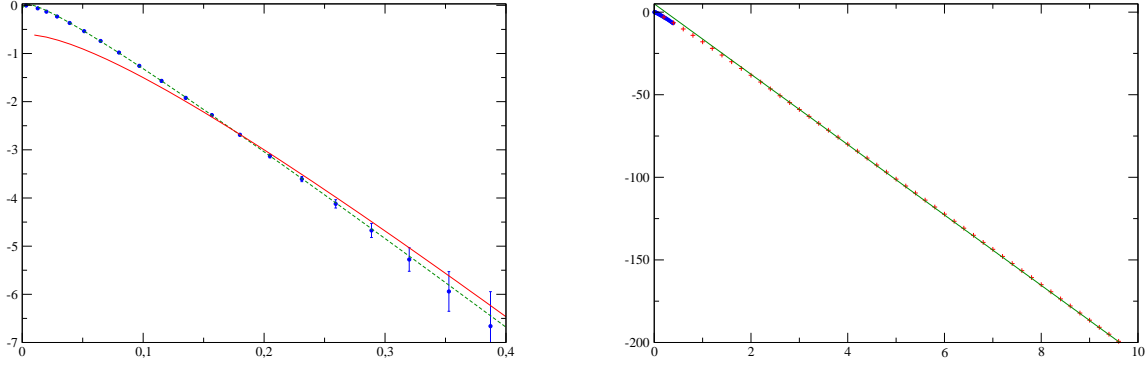
25

Figure 12: Left: Logarithm of rectangular Wilson loops with aspect ratio 1:2 as a function of the area for an ensemble with 500 instantons of variable size $\rho \leq 0.1$. The solid curve has been obtained from a fit of $\ln W$ in Eq. (70) to the data in Fig. 11 with the resulting values given in (71) while the dashed curve shows our standard fit (74) to the data points with aspect ratio 1:2 in the present figure with the extracted values (75). Right: Asymptotic extraction of the string constant from Wilson loops as a function of the area. Notice the much larger scale of the area. Crosses represent the function (70) with the values of the parameters (71). The straight line is obtained from fitting the asymptotics of (70) (crosses). The extracted value of the string tension is given in Eq. (76).

such that neither the asymptotic behavior at large area nor, for fixed area, at large perimeter is changed. In turn, the changes in fit parameters are very small [cf. Eq. (71)]

$$\lambda = 0.25, \ a = -0.7, \ b = 1.8, \ \sigma_0 = -13 \ . \tag{71}$$

As Fig. 11 demonstrates, the Ansatz (70) catches the essential properties of the pseudoparticle Wilson loops of sufficiently large size. Deviations at large values of the perimeter must be expected. The string picture breaks down if the smaller length R of the rectangle is of the order of the diameter of the flux tube,

$$R \approx 2r_0,$$

and therefore the perimeter has to satisfy

$$\mathcal{P} \leq \mathcal{P}_{\text{max}} = \frac{\mathcal{A} + 4r_0^2}{r_0} \ . \tag{72}$$

With $r_0 \approx 0.15 \, \text{fm}$ (corresponding to 0.07 in our units) we obtain for $\mathcal{A} = 0.15$ (second curve from the top in Fig. 11) $\mathcal{P}_{\text{max}} = 2.4$, a value which, as can be seen from Fig. 11, is of the correct order of magnitude.

The origin of the observed threshold behavior is not obvious. It could be a peculiarity of the effective regularization in pseudoparticle ensembles. Within the string model description, to lowest order, the string partition function [Eq. (67)] does not depend on the variable $|T - R|$. One can show that the derivative of the ζ function (66) with respect to the perimeter is finite at threshold. Infinite slopes of the Wilson loops however appear in higher order corrections which have been calculated in ζ function regularization [22]. It would be interesting to extend our analysis and include such corrections within heat kernel regularization.
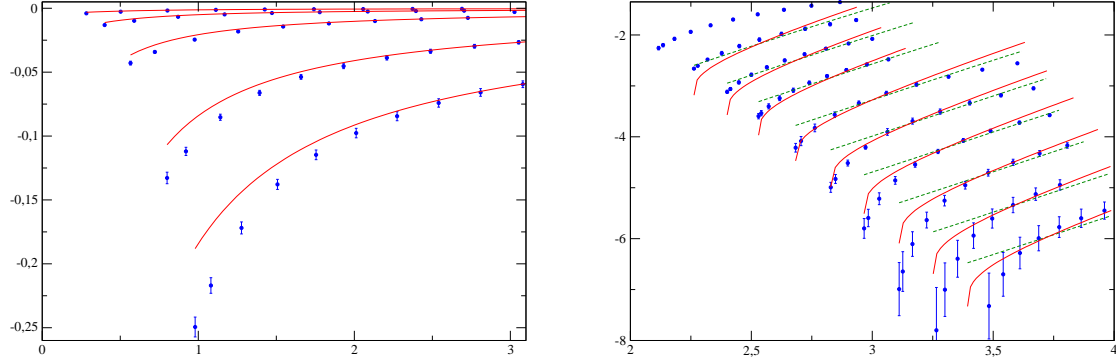
Figure 13: Logarithm of rectangular Wilson loops of fixed area as a function of the perimeter for an ensemble with 500 merons of variable size $\rho \leq 0.1$. Left: $\mathcal{A} = 0.005, 0.01, 0.02, 0.04, 0.06$. The curves are obtained from Eqs. (58, 59) with the value (77) of the regulator. Right: The 10 values of the area vary between 0.08 and 0.72. The dashed and solid curves are obtained from Eqs. (68) and (70) with the values of the parameters given in Eqs. (78) and (79), respectively.

Having determined the counterterms (71), we extract the value of the string constant σ from the asymptotic behavior of $\ln W$ [Eq. (70)]

$$\sigma RT = \lim_{RT \to \infty} -T \, F(\lambda) + \sigma_0 RT \,. \tag{73}$$

Fig. 12 illustrates the procedure. On the left hand side our standard procedure for determining the string constant by fitting the Wilson loop at constant aspect ratio (1:2) is shown. The fit with the standard Ansatz

$$\ln W = \omega + \tau \mathcal{P} - \sigma \mathcal{A} \tag{74}$$

and extracted values

$$\omega = -0.1, \ \tau = 0.58, \ \sigma = 20.5 \tag{75}$$

yields an excellent fit to our numerical results. The extracted value of the coefficient τ is about a factor two smaller than the slopes of the dashed curves in Fig. 11, and does not adequately describe the numerical results.

The Ansatz based on the string model (70), which also accounts for the dependence on the perimeter for fixed area, describes the pseudoparticle Wilson loops in a limited region only. Clearly the string model is not suited to describe the perturbative region of small loops. On the right hand side we show the extraction of the string constant from the asymptotics. Within the uncertainty of the procedures, the value

$$\sigma = 21 \tag{76}$$

agrees with the value in (75).

Very similar results are obtained for the Wilson loops in meron ensembles. In Fig. 13, the results of the analysis are presented for small and large Wilson loops respectively. The value of the heat kernel regulator for the small Wilson loops [cf. Eqs. (58,59)] is

$$\alpha = 0.20 \,. \tag{77}$$

27

The parameters for the string model Ansatz (68) have been determined to be

$$\lambda = 0.21, \ a = -1.2, \ b = 0.9, \ \sigma_0 = 0.8 \tag{78}$$

and for the modified Ansatz (70)

$$\lambda = 0.21, \ a = -1.1, \ b = 0.9, \ \sigma_0 = 1.3 \,. \tag{79}$$

The string tension extracted from the asymptotics of Eq. (70) is

$$\sigma = 12.5 \,, \tag{80}$$

in agreement with the value deduced from the parameterization (74)

$$\omega = -0.5, \ \tau = 0.94, \ \sigma = 12.8 \,. \tag{81}$$

The consistency of the results of these two different methods is an important indicator of the robustness of our determination of the string tension.

4.4 Wilson Loop Distributions and Higher Representation Wilson Loops

Wilson loop distributions and Wilson loops in higher representations further characterize the confining Yang-Mills dynamics. In particular, by lattice calculations, an intermediate regime of Casimir scaling has been established for both SU(2) and SU(3) Yang-Mills theories and deviations from Casimir scaling by string breaking have been identified, cf. [23, 24, 25, 26]. More recently, the Wilson loop distributions have been introduced [13] as quantities that contain the full information on the Wilson loops in higher representations. The study of Wilson loop distributions revealed an unexpectedly simple property of the Yang-Mills dynamics. These distributions can be described as a result of a diffusion process. Here we will present the Wilson loop distribution for pseudoparticle ensembles and discuss the related expectation values of Wilson loops in higher representations. We will compare our results with the diffusion model for the Wilson loop distribution. In this model the Wilson loop distribution $p(\cos\vartheta, t)$ is a solution of the diffusion equation on the group manifold S^3,

$$\left(\frac{\partial}{\partial t} - \Delta_{S^3}\right) \frac{p(\cos\vartheta, t)}{\sin\vartheta} = \frac{1}{\sin^2\vartheta} \, \delta(\vartheta)\delta(t) \,, \tag{82}$$

and is given by

$$p(\cos\vartheta, t) = \frac{2}{\pi} \, \theta(t) \sum_{n=1}^{\infty} n \, \sin n\vartheta \, e^{-(n^2-1)t} \,. \tag{83}$$

The diffusion model makes no assumption about the connection between the "time" t and the Wilson loop size. For given size of the loop, we determine the value of the time t by fitting the expectation value of the Wilson loop. As demonstrated in the left part of Fig. 14, the Wilson loop distributions are well described by the diffusion model. In particular, the change in shape from the strongly peaked distribution for small loops to the Haar measure for large loops is correctly reproduced. These results are very close to results obtained in lattice gauge calculations [13] and, together with our other results, strongly support the treatment of the Wilson loop dynamics in the pseudoparticle approach.
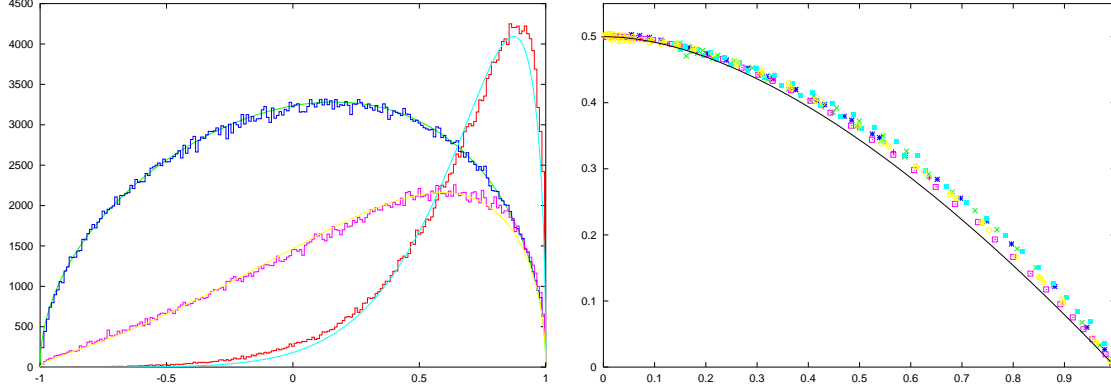
Figure 14: Left: Wilson loop distribution for an ensemble of configurations containing 500 merons. The sizes of the loops are $0.48 \times 0.24, 0.72 \times 0.36, 1. \times 0.5$ with average Wilson loop values $0.66, 0.26, 0.04$. These results are fitted with the distribution $p(\cos \vartheta, t)$ (83) with parameters $t = 0.13, 0.44, 1.05$ respectively. Right: Variance of the Wilson loop Δw (84) as a function of the average $\langle w \rangle$ for ensembles of merons with $N_M = 50, 100, 200, 500, 1000, 3200$ together with the results of the diffusion model Eq. (84).

Given the distribution of Wilson loops, the variance of Wilson loops is easily computed,

$$\Delta w = \sqrt{\langle w^2 \rangle - \langle w \rangle^2} = \frac{1}{2}\sqrt{1 - 4\langle w \rangle^2 + 3\langle w \rangle^{8/3}}, \tag{84}$$

as well as the expectation value

$$\langle W_j \rangle = e^{-4j(j+1)t} \tag{85}$$

of Wilson loops in the $(2j + 1)$-dimensional representation,

$$W_j(\vartheta) = \frac{1}{2j+1}\text{tr} \ \exp\left\{2i\vartheta \begin{pmatrix} -j & & \\ & \ddots & \\ & & j \end{pmatrix}\right\} = \frac{\sin(2j+1)\vartheta}{(2j+1)\sin\vartheta}. \tag{86}$$

The right hand side of Fig. 14 demonstrates the universality of the variance of the Wilson loop for meron ensembles with meron numbers N_M varying by up to a factor 60. Agreement with the diffusion model within 10% or less is found. The numerical results for Wilson loop expectation values in different representations are shown in Fig. 15 together with fits using the parameterization (49). With increasing dimensionality of the representation, the negative slope of the logarithm of the Wilson loop expectation values increases by about a factor 5 (cf. Table 4).

j	ω	τ	σ
1/2	-0.72	1.10	11.5
1	-0.99	1.89	24.5
3/2	-0.85	2.24	37.5
2	-0.96	2.95	54.5

Table 4: Parameters for the fit (49) of Wilson loops in the representation j for a meron ensemble with $N_M = 500$ ($\lambda = 1$).
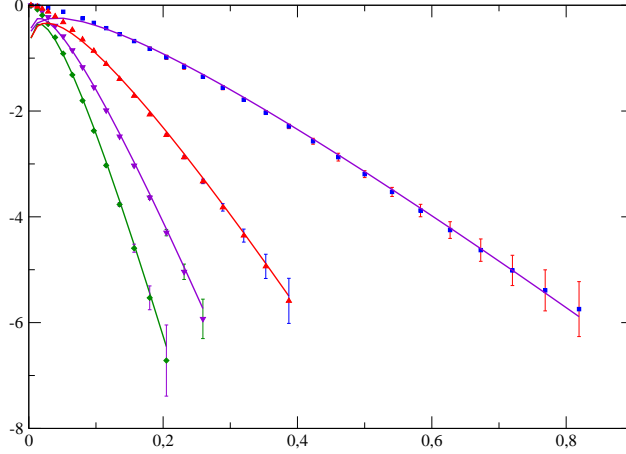
Figure 15: Logarithm of a Wilson loop as a function of its area for meron ensemble with $N_M = 500$ in $j = 1/2, 1, 3/2$, and 2 representations. Also shown are curves corresponding to the parameterizations (49) with the values of the parameters given in Table 4.

According to the diffusion model Eq. (85), Wilson loops in different representations exhibit Casimir scaling, i.e., the values of the string tension, or more generally the interaction energy of static charges in higher representations, are proportional to $j(j + 1)$. We have

$$R_j = \frac{\ln\langle W_{j+1}\rangle}{\ln\langle W_j\rangle} = \frac{(j + 1/2)(j + 3/2)}{j(j + 1)} \,. \tag{87}$$

Casimir scaling of the Wilson loops in two meron ensembles is examined in Fig. 16. On the average, we find that Casimir scaling is satisfied within 8%. We observe a decrease in R_j by about this amount. It appears that Casimir scaling is exact for small Wilson loops. Also these results are compatible with the findings in lattice gauge calculations where the validity of Casimir scaling has been demonstrated for SU(2) [21] and SU(3) [23] Yang-Mills theory. Indications for deviations from Casimir scaling for sufficiently large loops have been obtained in [24] and [25] and string breaking has been observed in [26]. Due to poor statistics in the computation of large loops, we have not been able to establish or rule out string breaking in the pseudoparticle ensembles.

5   Correlation Functions

Correlation functions are useful tools to study susceptibilities, response functions, and excitations of many particle systems and quantum field theories. In the case of Euclidean time, they also enable the measurement of the energies of low-lying excited states. In this section, we will use appropriately chosen operators to study the topological susceptibility and low glueball masses of our effective theory, and compare them with corresponding lattice results. We begin with a discussion of methodology, describe the operators used to probe the system, discuss several related theoretical issues, present results for the 0^+, 1^+, 1^-, 2^+, and 2^- glueballs, and discuss a correlation function that reflects confinement.
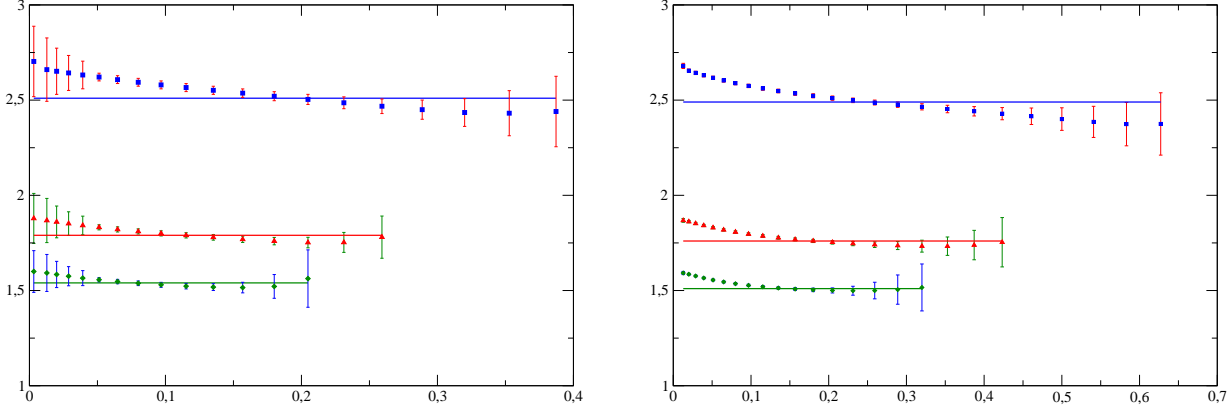
Figure 16: Ratios of logarithms of Wilson loops of merons in consecutive representations R_j [Eq. (87)] for $j = 1/2, 1, 3/2$, $N_M = 500$ (left) and $N_M = 200$ (right).

5.1 Correlation Functions of the Action- and Topological Charge Density

As an introduction, it is useful to begin by considering two correlation functions that we can analyze to a large extent analytically, the correlation functions of the action density [Eq. (2)],

$$C_s(x) = \langle [s(x) - \langle s \rangle][s(0) - \langle s \rangle] \rangle, \tag{88}$$

and of the topological charge density [Eq. (3)],

$$C_{\tilde{s}}(x) = \langle \tilde{s}(x)\tilde{s}(0) \rangle. \tag{89}$$

The action density $s(x)$ and topological charge density $\tilde{s}(x)$ are the simplest examples of gauge invariant quantities. They are scalar or pseudoscalar quantities and bilinear in the field-strength. The explicit expressions of these quantities for a single meron or instanton are given in Eqs. (7) and (8). The normalization of the correlation functions yields the variance of the action and topological density respectively. Many results from this section have been tabulated in Tables 2 and 3 for previous reference and discussion, and one can see from these tables that fluctuations of the action are of the same order as the average value,

$$\sqrt{C_S(0)} \sim \langle s \rangle.$$

The large fluctuations are due to the large differences in the values of the action density inside the pseudoparticles and in the background. In the center,

$$s_0(0) = \tilde{s}_0(0) = \frac{12\xi^2}{\rho^4}$$

which, in the ensemble of fields with 500 merons for example, is an order of magnitude larger than the average action density. The square of the action and of the topological density is concentrated in the core of the pseudoparticles. Therefore the strength of the fluctuations and

31

more generally the correlation function can be estimated by the incoherent sum over the single pseudoparticles. In such an incoherent single pseudoparticle approximation, we define the correlation function of, for instance, the topological density by

$$
C_{\tilde{s}}^{\text{incoh}}(x) = \frac{1}{V} \sum_{i=1}^{N_P} \int \mathrm{d}^4 z_i \, \tilde{s}_0(y - z_i) \, \tilde{s}_0(y + x - z_i) = \frac{N_P}{V} \int \mathrm{d}^4 y \, \tilde{s}_0(y) \, \tilde{s}_0(y + x) \,, \quad (90)
$$

and similarly for any other observable. In this approximation, the integration over the color orientation gives a multiplicative factor which is canceled by the normalization of the partition function. Using the explicit expressions (7) and (8), we obtain the following estimates for the fluctuations in meron ensembles ($N = N_M$)

$$
C_s^{\text{incoh}}(0) = \frac{1551\pi^2}{280} \frac{N_M}{\rho^4 \, V} \,, \quad C_{\tilde{s}}^{\text{incoh}}(0) = \frac{177\pi^2}{35} \frac{N_M}{\rho^4 \, V} \,, \quad \xi = 1 \,, \quad (91)
$$

and for instantons

$$
C_s^{\text{incoh}}(0) = C_{\tilde{s}}^{\text{incoh}}(0) = \frac{384\pi^2}{7} \frac{N_I}{\rho^4 \, V} \,, \quad \xi = 2 \,. \quad (92)
$$

Comparison with the numerical results in Tables 2 and 3 shows that the general trends in the values of the correlation functions for vanishing separation are correctly reproduced by this incoherent superposition of pseudoparticles. The similar values of $C_s(0)$ and $C_{\tilde{s}}(0)$, the difference by an order of magnitude for meron and instanton ensembles, the dependence on the pseudoparticle size and number density agree typically within 20-30 % with the numerical results. Although the pseudoparticle ensembles are far from being random, the fluctuations are dominated by the variations of the densities on the small scale of the meron size where the longer range correlations between pseudoparticles have little effect.

In the following, we will compare our numerical results for the correlation function with the single pseudoparticle predictions [cf. Eq. (90)] which we have evaluated numerically for various observables. Besides the values for zero separation [Eqs. (91, 92)], the asymptotic behavior can also be determined analytically. We find for meron ensembles

$$
t \to \infty : \quad C_s^{\text{incoh}}(t) \to \frac{9\pi^2}{2} \frac{N_m}{V} \frac{\ln t/\rho}{t^4} \,, \quad C_{\tilde{s}}^{\text{incoh}}(t) \to 24\pi^2 \frac{N_M}{V} \frac{\rho^2}{t^6} \,, \quad \xi = 1 \,, \quad (93)
$$

and for instanton ensembles

$$
t \to \infty : \quad C_s^{\text{incoh}}(t) = C_{\tilde{s}}^{\text{incoh}}(t) \to 24\pi^2 \frac{N_I}{V} \frac{\rho^4}{t^8} \,, \quad \xi = 2 \,. \quad (94)
$$

The integral over the topological charge density correlation function yields the topological susceptibility

$$
\chi = \left(\frac{1}{8\pi^2} \right)^2 \int \mathrm{d}^4 x \, C_{\tilde{s}}(x) \,, \quad (95)
$$

an important quantity of the strong interaction. In Tables 2 and 3 the values of $\chi^{1/4}$ for the various ensembles are given. Once more, these values essentially arise from an incoherent sum of single pseudoparticle contributions. For the calculation of χ we need the curvature β,

$$
\beta = -\frac{(C_{\tilde{s}}(0))''}{2 C_{\tilde{s}}(0)} = -\frac{1}{2 C_{\tilde{s}}(0)} \int \mathrm{d}^4 x \, \tilde{s}(x) \, \partial_t^2 \, \tilde{s}(\mathbf{x}, t) \,,
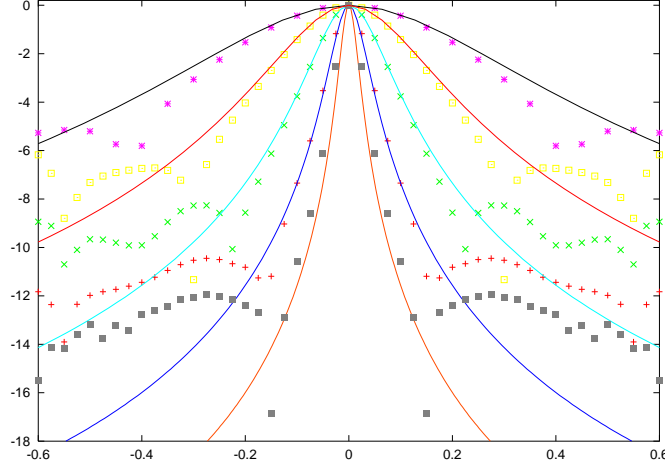$$

32

Figure 17: The correlation function $|C_{\tilde{s}}(x)|$ for $N_M = 50$, $\rho = 0.01, 0.02, 0.04, 0.08, 0.16$ in comparison with the single-meron correlation functions. Note that in every case the correlation function has a node beyond which it is negative.

and by approximating the single pseudoparticle correlation function by a Gaussian of the same curvature we obtain

$$\chi^{1/4} = \sqrt{\frac{1}{8\pi\beta}}\, C_{\tilde{s}}(0)^{1/4}$$

resulting in

$$\beta^{\text{incoh}} = \frac{184}{177}\frac{1}{\rho^2}\,, \quad \xi = 1\,; \quad \beta^{\text{incoh}} = \frac{4}{3\,\rho^2}\,, \quad \xi = 2\,, \tag{96}$$

and the following expressions for meron and instanton ensembles

$$\left(\chi^{\text{incoh}}\right)^{1/4} = 0.52\left(N_M/V\right)^{1/4}\,, \quad \xi = 1\,; \quad \left(\chi^{\text{incoh}}\right)^{1/4} = 0.83\left(N_I/V\right)^{1/4}\,, \quad \xi = 2\,. \tag{97}$$

The $N^{1/4}$ dependence is easily understood on rather general grounds. If we assume the topological charge in volume V to be given by the difference in the number of pseudoparticles and anti-pseudoparticles $N - \bar{N}$, the fluctuation in the charge is expected to be $\sim \sqrt{N_M}$ and hence $\chi \sim N$. The estimate (97) deviates from the numerical results by about 10 %. For small pseudoparticle sizes, the approximation of the distribution by a Gaussian becomes invalid and deviations of the order of 20-30 % occur.

The case of the topological charge density correlation function is particularly interesting. Since $\tilde{s} \sim E \cdot B$, it acquires an i in Euclidean space and the correlation function is negative for nonzero x, $C_{\tilde{s}}(x) \sim -\sum_n |\langle 0|\tilde{s}|n\rangle|^2 \mathrm{e}^{-E_n x}$. The positive topological susceptibility arises from a positive contact term at at the origin [27]. As Fig. 17 shows, the pseudoparticle approximation to the path-integral exhibits these properties. The contact term is approximated by the single pseudoparticle distribution [Eq. (90)], and after the change of sign, the correlation function exhibits a new length scale. For $\rho = .02$, the results follow the single meron correlation function until $\tilde{s}(x)$ has decreased to a value of about $5 \cdot 10^{-5}$. Only at this level does a new length scale become important. We see here in detail how with decreasing cutoff ρ, the strength remains in the short range peak to produce a topological susceptibility essentially independent of the value of the cutoff.
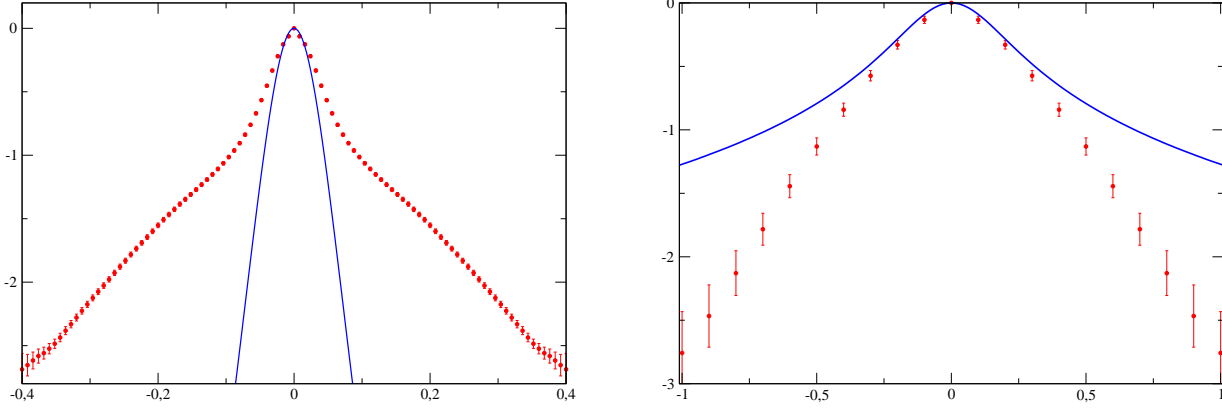
Figure 18: Emergence of the hadronic scale in the correlation function $C_s(x)$ in ensembles with 50 instantons of size $\rho = 0.05$ (left) and 800 merons ($L = 4$) of size $\rho = 0.2$ (right), in comparison with the respective single pseudoparticle correlations functions.

In section 4, we have already compared the measured topological susceptibilities for instanton and meron ensembles with lattice results. The instanton result, $0.42 \le \chi^{1/4}/\sigma^{1/2} \le 0.48$, agrees within roughly 10% with the SU(2) lattice result [19], whereas the meron result $\chi^{1/4}/\sigma^{1/2} \approx 0.31$ is significantly lower. From the developments in this section, we now see the origin of this difference. The estimate (97) of the ratio of 1.6 of the topological susceptibilities ($\chi^{1/4}$) of instantons and merons arises from the fact that the topological charge of instantons is twice that of merons, and this ratio is only slightly reduced when expressed in physical units. Fig. 18 shows results for the action density correlation function that illustrate the emergence of a hadronic scale, that is, a scale generated by dynamics that is significantly different from the scale set by the size of the pseudoparticles. If an effective theory has the correct degrees of freedom, we should expect it to be able to generate scales larger or smaller than that of the underlying pseudoparticles. The left figure demonstrates the superposition of instantons of small size ($\rho = 0.05$ fm) to generate a much larger correlation length, a familiar phenomenon arising in many-body systems. The right figure shows an example of the opposite case, where superimposing merons of size 0.2 fm actually generates a hadronic scale that is smaller than the meron size. To emphasize the very slow decay [cf. Eq. (93)] of the single meron correlation function, its profile is also shown in the figure. The emergence of the hadronic scale is a rather subtle effect generated by destructive interference among the pseudoparticles. To demonstrate the dominance of this hadronic scale over a large distance despite the weak decay of the building blocks, we had to use a meron ensemble in a volume 16 times larger than usual and containing 16 times more pseudoparticles.

The successful generation of the negative correlation function for the topological charge density and of hadronic scales both larger and smaller than the pseudoparticle scales for the action density are important indicators of the potential of the pseudoparticle effective theories to describe low energy dynamics. Based on this success, we now use correlation functions to explore the low lying glueball spectrum.

5.2 Correlation Functions and Glueball Masses

To the extent to which the effective degrees of freedom succeed in representing the full path integral, the integration yields a transfer matrix and one may write a Euclidean correlation function as a sum over eigenstates,

$$\langle \mathcal{O}(x)\mathcal{O}(0)\rangle \sim \sum_n \langle \Omega|\mathcal{O}|n\rangle \mathrm{e}^{-E_n x}\langle n|\mathcal{O}|\Omega\rangle \,. \tag{98}$$

As in lattice gauge theories, glueball masses may be extracted from the exponential decay at sufficiently large distances. In the case of the action density, we thus expect for large separation x that $C_s(x) \sim |\langle n_0|s|0\rangle|^2 \mathrm{e}^{-m_0 x}$, where m_0 is the mass of the lowest 0^{++} glueball. Similarly, the asymptotic decay of the pseudoscalar correlation function is expected to be determined by the lowest 0^{-+} glueball mass.

5.2.1 Methodology

To facilitate the extraction of single exponential terms in Eq. (98), it is advantageous to project onto states with zero momentum so that the continuum of states of non-zero momentum associated with each intrinsic excited state is eliminated, and the gap between the desired state and the next higher energy state is as large as possible. In addition, although in a rigorously translationally invariant system it would be sufficient to project either the source operator at the time origin or the sink operator at t, since the current calculation is only approximately translationally invariant, it is beneficial to project both the source and the sink. Hence, we will use the doubly momentum projected correlation functions

$$\hat{C}_{\mathcal{O}}(t) = \int_V \mathrm{d}^3x \int_V \mathrm{d}^3y \langle 0|\mathcal{O}(t,\mathbf{x})\mathcal{O}(0,\mathbf{y})|0\rangle \,. \tag{99}$$

The time direction in 4-dimensional space is defined here by the coordinate over which one does not integrate. The integration over the 3-dimensional cube V is limited to $\ell \approx 0.5L...0.7L$ in order to avoid surface effects.

In order to accurately determine glueball masses, it is necessary to identify a substantial region of pure exponential decay between short distance artifacts associated with the intrinsic size ρ of our effective degrees of freedom and large distance artifacts associated with the finite volume edge effects and the fact that beyond some point the fluctuations arising from finite statistics are comparable with the magnitude of the decaying exponential. In general, the region between the short distance and large distance artifacts is quite limited, and the identification of the exponential regime is ultimately subjective. Unfortunately, this precludes quantifying statistical and systematic errors, and in the following discussion we will simply explain our rationale for selecting the fiducial regions we use to extract the slopes defining the exponential decay of each state, and give representative values, or ranges of values for each slope. Fig. 18 is a good example of a case in which there is clear separation between the short range artifacts associated with the intrinsic size ρ and a substantial region of nearly exponential decay. Similarly, in Fig. 17, as previously noted, one observes the expected negativity in $C_{\tilde{s}}(x)$ beyond 2ρ, indicating that one is beyond the range of short distance artifacts. However, in this case, it is also clear that the

fluctuations become so large at larger distances that there is no correspondingly clean region of exponential decay, and we are not able to extract a mass from the pseudoscalar correlation functions in the present work.

Given the difficulties in determining masses in many cases, we have also required that we obtain consistent results ($< \pm 10\%$) for ensembles with different meron sizes or ensembles with different number of pseudoparticles. When possible, we have also used different operators to create states of the same quantum numbers, and sought consistency between these results. Finally, for spin 1 and 2 excitations we required deviations from rotational invariance to be small in the fiducial region.

5.2.2 Operators

To calculate glueball masses, we use correlation functions based on two kinds of operators: local operators constructed from products of two or three field-strength operators, and non-local Wilson loop operators. They are closely related to gluonic operators used in recent lattice calculations of the glueball spectrum and matrix elements (see [28] for the relationship to the lattice symmetry group and further refinements). We first introduce the local operators and discuss their behavior under interchange of Euclidean space and time axes, and then describe the Wilson loop operators. Properties of the operators and calculations based on them are summarized in Table 5.

Local operators with two or three field-strengths

We have considered the complete set of gauge invariant operators consisting of products of 2 or 3 field-strength operators, which we represent in terms of magnetic and electric fields in order to make the transformation properties under 3-rotations explicit. We use the following set of observables consisting of two field operators

$$s = \frac{1}{4}(\mathbf{E}^2 + \mathbf{B}^2)\,, \ \ T_+ = \mathbf{E}\otimes\mathbf{E} + \mathbf{B}\otimes\mathbf{B}\,, \ \ T_- = \mathbf{E}\otimes\mathbf{E} - \mathbf{B}\otimes\mathbf{B}\,, \ \ T_a = \mathbf{E}\otimes\mathbf{B} + \mathbf{B}\otimes\mathbf{E}\,, \ \ (100)$$

with the traceless tensors

$$(\mathbf{X}\otimes\mathbf{Y})_{ij} = X_i^a Y_j^a - \frac{1}{3}\mathbf{X}^a\mathbf{Y}^a\delta_{ij}\,, \tag{101}$$

and the following observables consisting of products of 3 field-strengths

$$\begin{aligned} \mathbf{V}_p &= \ \epsilon^{abc}(\mathbf{E}^a \cdot \mathbf{B}^b)\,\mathbf{B}^c\,, \ \ \mathbf{V}_a = \epsilon^{abc}(\mathbf{E}^a \cdot \mathbf{B}^b)\,\mathbf{E}^c\,, \\ T_3 &= \ \epsilon^{abc}[(\mathbf{B}^a \times \mathbf{B}^b)\otimes\mathbf{E}^c + \mathbf{E}^c\otimes(\mathbf{B}^a \times \mathbf{B}^b)]\,. \end{aligned} \tag{102}$$

To improve the statistics we have summed the correlation functions for vectors and tensors over the spatial components, e.g.

$$\langle(\mathbf{X}\otimes\mathbf{Y})(x)(\mathbf{X}\otimes\mathbf{Y})(y)\rangle = \sum_{j\geq i=1}^{3} \langle(\mathbf{X}\otimes\mathbf{Y})_{ij}(x)(\mathbf{X}\otimes\mathbf{Y})_{ij}(y)\rangle$$

and have used the equality of the components as a test for rotational invariance of the ensembles.

Our subsequent calculations all refer to instanton ensembles, for which the fiducial interval for extracting masses is larger. In cases where masses could be extracted from both kinds of ensembles, the results agreed within the uncertainty of the procedure. We observe that the instanton fields [Eqs. (5, 6)] satisfy

$$B_i^a = E_i^a = -4\frac{1}{(x^2 + 1)^2}\delta_{ai} \,.$$

As a consequence, gauge invariant combinations consisting of products of two or three field-strength operators have to be either scalar or pseudoscalar. For merons this is only true after momentum projection. If the momentum projection is not complete, the presence of single meron contributions will complicate the analysis of the correlation functions.

In addition to the action density and the three tensors [cf. Eq. (100)], we can form a second scalar, $\mathbf{B}^2 - \mathbf{E}^2$, the Hamiltonian density transformed to Euclidean space, and the Poynting vector, $\mathbf{E} \times \mathbf{B}$. Although if integrated over all space, the vacuum is an eigenstate of the resulting operators, our ensembles of pseudoparticles do not yield exact eigenstates of the Hamiltonian and projection to zero momentum is not exact. Hence, we obtain non-vanishing correlation functions. However, we find that the fluctuations in the Hamiltonian, i.e., the value of the correlation function for vanishing $|t|$, are one to two orders of magnitude smaller than those of the action, depending on the ensemble. In the case of the integrated Poynting vector, the momentum operator, we find very strong dependence of the correlation functions on the parameters of the ensembles, which highlights the unphysical origin of the correlations. For these reasons we do not consider these correlations further. Finally we remark that the "singular" behavior (cf. Fig. 17) of the pseudoscalar $(\mathbf{E} \cdot \mathbf{B})$ correlation function $C_{\tilde{s}}$ prevents a meaningful extraction of a mass after momentum projection.

Behavior under interchange of Euclidean space and time axes

In order to understand some of the results obtained subsequently, it is useful to note that by relativistic covariance, electric and magnetic fields can be transformed into each other. For vanishing separation, the distinction between electric and magnetic field depends on the choice of the coordinate system. We illustrate the equivalence by considering the following contribution to the correlation function of T_a

$$\langle t_{ij}(x_4)\rangle = \langle B_i E_j(\mathbf{0}, x_4)\, B_i E_j(0)\rangle = \langle \tilde{F}_{4i}F_{4j}(\mathbf{0}, x_4)\, \tilde{F}_{4i}F_{4j}(0)\rangle \,.$$

Here color indices are suppressed and no summation over i and j is carried out. Under a transformation which rotates the x_4 and x_i coordinates into each other

$$R: \ x_i \to x_i' = -x_4, \quad x_4 \to x_4' = x_i \tag{103}$$

we find, assuming 4-dimensional rotational invariance in the ensembles

$$R: \ \langle t_{ij}(x_4)\rangle = \langle \tilde{F}_{4i}F_{ij}(x')\, \tilde{F}_{4i}F_{ij}(0)\rangle, \quad x_k' = \delta_{ki}x_4, \quad i \neq j \,. \tag{104}$$

For vanishing separation ($x_4 = 0$), this result, if expressed by electric and magnetic fields

$$\langle B_i E_j(0)\, B_i E_j(0)\rangle = \sum_{k=1}^{3}\epsilon^{ijk}\langle B_i B_k(0)\, B_i B_k(0)\rangle, \quad i \neq j \,. \tag{105}$$

together with the definition (100) of the relevant tensors is seen to yield the identity

$$C_{T_+}(0) = C_{T_a}(0) \tag{106}$$

for the off-diagonal elements. The diagonal elements of the traceless tensor can be connected to the off diagonal ones by rotations not involving the 4-coordinates. We note that the rotation (103) has no counterpart in Minkowski space. This method is not directly applicable for non-vanishing separations since electric and magnetic fields are defined with respect to the direction of separation chosen as time axis

$$E_\nu = \hat{z}_\mu F_{\mu\nu}\,, \quad B_\nu = \hat{z}_\mu \tilde{F}_{\mu\nu}\,.$$

Here z denotes the 4-vector defining the separation and $\hat{z}$ the corresponding unit vector. Only with this definition electric and magnetic field do not mix under 3-dimensional rotations in the space transverse to the direction of separation, i.e., under rotations satisfying

$$R_{\mu\nu}z_\nu = z_\mu\,.$$

In this way the resulting operators project on states with definite angular momentum and parity. This redefinition invalidates the above derivation for finite separations. More complicated relations between the two correlation functions can be derived which however defy a direct numerical application. As we discuss below, it is striking that our numerical results for the two momentum projected correlation functions $C_{T_+}(x)$ and $C_{T_a}(x)$ exhibit essentially identical normalizations and a strong similarity in shape. Significant deviations occur only at the level of about 0.01 of the value at zero separation. It would be interesting to investigate these correlation functions in lattice calculations. In the derivation of the identity (106), we made use of the transformation properties of the field-strength under rotations by 90 degrees, and one may therefore expect that such relations remain valid on the lattice with the discrete symmetry of a hypercube.

It will also be important subsequently to note the close relationship of T_- to the Poynting vector. Using the same arguments as above, it follows that the off-diagonal matrix elements T_- are related to the Poynting vector by the rotation (103)

$$\mathbf{P} = \mathbf{E}^a \times \mathbf{B}^a\,,$$

with the consequence that

$$C_{T_-}(0) = \langle T_{-ij}(0)T_{-ij}(0)\rangle = \sum_{k,l=1}^{3} \epsilon^{ijk}\epsilon^{ijl}\langle P_k(0)P_l(0)\rangle \quad i \neq j\,, i,j \text{ fixed.} \tag{107}$$

Wilson loop operators

In addition to the local operators discussed above, it is also interesting to consider correlation functions of Wilson loops. This will enable us to investigate the role of the locality of the operator in the determination of the glueball masses and to make contact with the operators used in lattice gauge calculations.

We denote the direction in which the Wilson loops are separated as time direction and will perform weighted spatial averages of the Wilson loops in order to project on states of definite

spin. We consider circular loops of radius r and denote the unit vector normal to the plane of the circle by $\mathbf{n}$ and the coordinate of the center of the circle by $\mathbf{x}_0$,

$$W_r(\mathbf{n}, \mathbf{x}_0, t) = \frac{1}{2} \operatorname{Tr} \mathbf{P} \, e^{ig \oint A_\mu(x) dx^\mu}. \tag{108}$$

If applied to the vacuum, this operator generates states of different momenta and different spins. Projection of $W(\mathbf{n}, \mathbf{x}_0, t)$ on definite spin ℓ, m is obtained by

$$W_r^{\ell m}(\mathbf{x}_0, t) = \int d\Omega_\mathbf{n} W_r(\mathbf{n}, \mathbf{x}_0, t) \, Y_{\ell m}^*(\mathbf{n}) \tag{109}$$

and on zero momentum by spatial averaging

$$W_r^{\ell m}(t) = \frac{1}{V} \int d^3 x_0 W_r^{\ell m}(\mathbf{x}_0, t). \tag{110}$$

Translational invariance in Euclidean 4-space and 3-dimensional rotational invariance impose constraints on the correlation functions. We have

$$\langle (W_r^{\ell m}(t) - \langle W_r^{\ell m}(t) \rangle)(W_r^{*\ell' m'}(t') - \langle W^{*\ell' m'}(t') \rangle) \rangle$$
$$= \delta_{\ell\ell'}\delta_{mm'} \left[\langle W_r^\ell(t - t') W_r^\ell(0) \rangle - \langle W_r^\ell \rangle^2 \delta_{\ell,0} \right] = C_\ell(t - t') \, \delta_{\ell\ell'}\delta_{mm'}. \tag{111}$$

We have used the fact that by rotational and translational invariance the correlator

$$\langle \int d^3 x_0 \, W_r(\mathbf{n}, \mathbf{x}_0, t) \int d^3 y_0 \, W_r^*(\mathbf{n}', \mathbf{y}_0, t') \rangle = W_r(\mathbf{n} \cdot \mathbf{n}', t - t') \tag{112}$$

can depend only on the angle between the two orientations of the Wilson loops. Similarly

$$\langle (W_r^{\ell m}(\mathbf{x}_0, t) - \langle W_r^{\ell m}(\mathbf{x}_0, t) \rangle)(W_r^{*\ell' m'}(\mathbf{x}_0, t') - \langle W^{*\ell' m'}(\mathbf{x}_0, t) \rangle) \rangle = D_\ell(t - t')\delta_{\ell\ell'}\delta_{mm'}. \tag{113}$$

We finally observe that [cf. Eq. (108)]

$$W_r(\mathbf{n}, \mathbf{x}_0, t) = W_r(-\mathbf{n}, \mathbf{x}_0, t), \tag{114}$$

and therefore the correlation functions (113, 114) vanish for odd ℓ.

In order to improve the statistics, we actually do not make use of the m-independence of the correlation functions but rather sum over all values of m in Eqs. (111) and (112). In order to relate the Wilson loop correlation functions to the field-strength correlation functions, we consider the limit of small size Wilson loops, i.e., $r \ll \rho$. In this limit and for fixed orientation $\mathbf{n}$ we have

$$r \to 0 : \quad W_r(\mathbf{n}, \mathbf{x}_0, t) = g^2 \pi^2 r^4 (\mathbf{n} \cdot \mathbf{B}^a(\mathbf{x}_0, t))^2. \tag{115}$$

Integration over the orientation [Eq. (109)] yields

$$r \to 0 : \quad W_r^{0,0}(\mathbf{x}_0, t) = \frac{\sqrt{4\pi}}{3} g^2 \pi^2 r^4 (\mathbf{B}^a(\mathbf{x}_0, t))^2, \tag{116}$$

whereas the $\ell = 2$ projection gives, for instance, for the $m = 0$ component

$$r \to 0 : \quad W_r^{2,0}(\mathbf{x}_0, t) = \frac{\pi}{10} g^2 \pi^2 r^4 [(B_3^a(\mathbf{x}_0, t))^2 - \frac{1}{3}(\mathbf{B}^a(\mathbf{x}_0, t)^2)]. \tag{117}$$

As expected, at small sizes, the angular momentum projected operators reduce for $\ell = 0$ to $(\mathbf{B}^a)^2$ and for $\ell = 2$ to $\mathbf{B} \otimes \mathbf{B}$,

$$(\mathbf{B} \otimes \mathbf{B})_{ij} = B_i^a B_j^a - \frac{1}{3}\mathbf{B}^a\mathbf{B}^a\delta_{ij} = \frac{1}{2}(T_+ - T_-)_{ij} \, . \tag{118}$$

Electric field operators do not appear since the Wilson loops considered are located in spatial planes $(\mathbf{e}_4 \cdot \mathbf{A^a} = 0)$.

For subsequent reference, all the operators used to calculate correlation functions, salient properties, and the results of measurements are summarized in Table 5.

state	name	operator	$x_i \leftrightarrow x_4$	figures (slope)
0^+	S	$1/4(\mathbf{E}^2 + \mathbf{B}^2)$		21 (-4.0)
0^+	W_r^{00}	$\int d\Omega_{\mathbf{n}} W_r(\mathbf{n}, \mathbf{x}_0, t)\, Y_{00}^*(\mathbf{n})$		27 (-)
1^-	$\mathbf{V}_p$	$\epsilon^{abc}(\mathbf{E}^a \cdot \mathbf{B}^b)\, \mathbf{B}^c$		26 $(-9 \dots -10)$
1^+	$\mathbf{V}_a$	$\epsilon^{abc}(\mathbf{E}^a \cdot \mathbf{B}^b)\, \mathbf{E}^c$		26 $(-10.5 \dots -11)$
2^+	W_r^{2m}	$\int d\Omega_{\mathbf{n}} W_r(\mathbf{n}, \mathbf{x}_0, t)\, Y_{2m}^*(\mathbf{n})$		27 $(-7.5 \dots -7.8)$
2^+	T_-	$\mathbf{E} \otimes \mathbf{E} - \mathbf{B} \otimes \mathbf{B}$	$\mathbf{P} = \mathbf{E}^a \times \mathbf{B}^a$	20 (-), 23 (-), 24 (-)
2^+	T_+	$\mathbf{E} \otimes \mathbf{E} + \mathbf{B} \otimes \mathbf{B}$	T_a	19 (-8.0), 23 (-)
2^+	T_a	$\mathbf{E} \otimes \mathbf{B} + \mathbf{B} \otimes \mathbf{E}$	T_+	20 (-), 22 (-8.3), 23 (-)
2^-	T_3	$\epsilon^{abc}[(\mathbf{B}^a \times \mathbf{B}^b) \otimes \mathbf{E}^c + \mathbf{E}^c \otimes (\mathbf{B}^a \times \mathbf{B}^b)]$		25 (-9.3)

Table 5: Summary of operators used to calculate glueball masses and the results of measurements. The slope, specifying the glueball mass, for each figure is shown in parentheses.

5.2.3 Correlation Functions of Field-Strength Operators

With the preceding definitions and discussion, we now present the results of our calculations of correlation functions in instanton ensembles.

T_+

We begin with the correlation function of the 2^+ operator T_+ [cf. Eq. (100)] in Fig. 19. For small separations, the shape of the correlation function (curvature) still reflects the size of a single instanton, even though the single instanton correlation functions vanishes. Now the instanton size appears at small separations via the interference of some "mean-field" with the gauge field of a single instanton. In the intermediate regime $.2 \leq |t| \leq .6$ approximately, a common slope can be associated with the correlation functions in these various ensembles. In this particular case of the T_+ correlation function, we extract a slope of 8. For larger separations we observe strong fluctuations in the correlation functions. As is shown in the lower part of the figure, these fluctuations are connected to violations of the rotational symmetry. After reducing the diagonal components of the tensor by 1/3, all 6 components of the tensor are identical if the ensemble exhibits exact rotational symmetry. Comparison of the two figures strongly suggest that the differences in the correlation functions for the different ensembles for $|t| > .5 - .6$ are a consequence of the violations of the rotational symmetry in the individual ensembles.
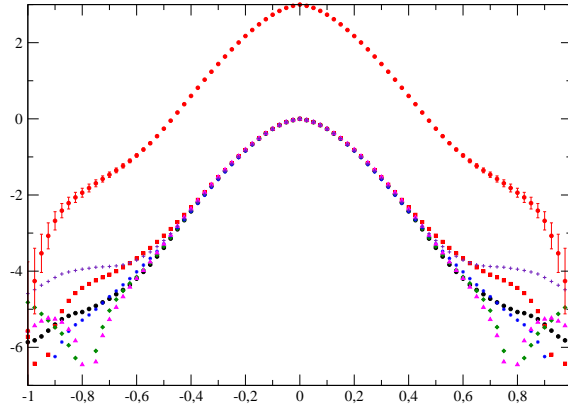
Figure 19: Summed correlation function of T_+ [Eq. (100)] and its decomposition into its 6 components (denoted by different symbols) T_{+ij}, $i \leq j$ in an ensemble with 50 instantons of variable size.

As a further consistency check we also have compared correlation functions of ensembles which differ in the number of pseudoparticles. In Fig. 20 we have rescaled the values of t for the
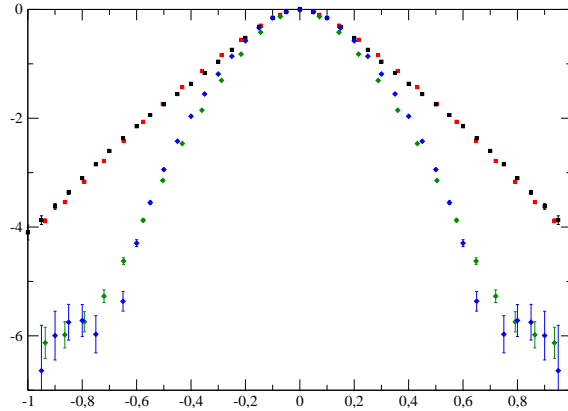

Figure 20: Demonstration of scaling of the T_- (red and black squares, upper curves) and T_a (green and blue diamonds, lower curves) correlation function for ensembles with 50 and 200 instantons of size $\rho = 0.16$.

correlation function of the ensemble with 50 instantons by a factor 1.44 as suggested by the analysis of the Wilson loops (cf. Table 3). As is seen, the extracted slopes or masses scale as expected with $\sqrt{\sigma}$ within 10% or better.

S

The intermediate states contributing to the correlation functions of the action density are 0^+ states. Difficulties arise in the numerical evaluation of this correlation function due to the large contribution from the intermediate ground state. The subtraction of the vacuum expectation
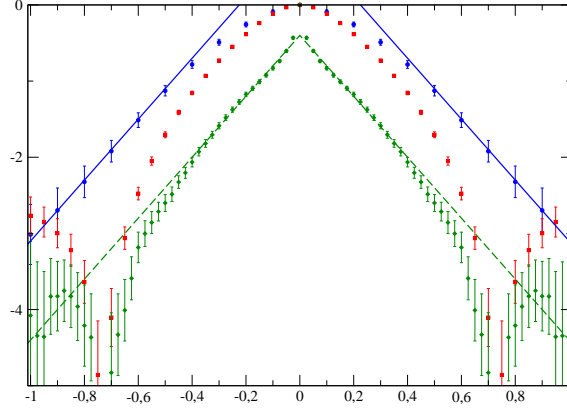
Figure 21: Action density correlation function $C_s(x)$ of ensembles with 50 instantons of size $\rho = 0.16$ (red squares), $\rho = 0.04$ (green diamonds), and 800 instantons ($L = 4$) of size $\rho = 0.16$ (blue circles). The slope of the straight lines is -4.0.

value [cf. Eq. (88)] makes the correlation function C_s particularly sensitive to the violations in translational and rotational symmetry. A stable and unambiguous result could be obtained only by constructing ensembles in a larger volume in which the violation of translational invariance is significantly weaker. We have used the ensemble of pseudoparticles discussed above in the context of the thermodynamic limit and calculated the action density correlation function in a 16 times larger volume with 800 pseudoparticles. The result of this calculation is shown in Fig. 21.
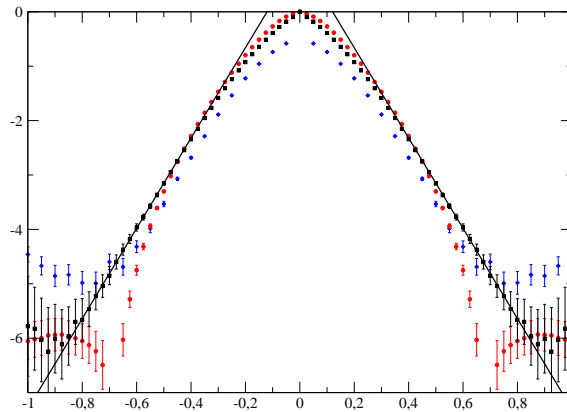
Figure 22: Correlation function of T_a for different ensembles. 800 instantons ($L = 4$) of size $\rho = 0.04$ (blue diamonds), 50 instantons of size $\rho = 0.04$ (black squares) and of variable size (red circles). The value of the slope is -8.3.

Unlike for the other correlation functions, very different results are obtained for the action density correlation in the two "equivalent" ensembles. We note that the correlation function in the

small volume displays a zero at $|t| = 0.75$ independent of the instanton size. In the larger volume, these fluctuations violating translational invariance are reduced resulting in a reasonable behavior of the correlation function. As illustrated in Fig. 21 for sufficiently small instanton sizes, where the single instanton contribution is restricted to small separations, a fiducial interval exists where a meaningful value of the mass can be extracted also in the ensemble with the smaller volume, and we indeed obtain the same slope.

T_+, T_-, T_a

The correlation functions of the 3 tensor operators bilinear in the field-strength [cf. Eq. (100)]
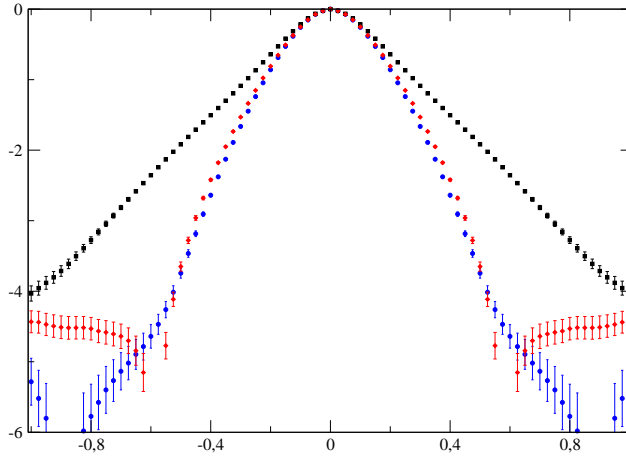
Figure 23: Tensor correlation functions T_+ (blue circles), T_- (black squares), and T_a (red diamonds) of an ensemble with 50 instantons of size $\rho = 0.1$.

with the 2^+ ($T_\pm$) and 2^- (T_a) excitations appearing as intermediate states are shown in Fig. 23. Surprisingly, not the correlation functions of operators with the same but rather those with opposite parity are very similar in shape and actually possess the same normalization. Our numerical results yield $C_{T_+}(0) = C_{T_a}(0)$ within the statistical accuracy and furthermore, this equality persists at finite separation within a few percent for the corresponding values of the momentum projected (99) correlation functions. As discussed in the previous section, the equality at zero separation follows from Eq. (106), arising from the equivalence of the two operators under interchange of x_t and x_i.

We now turn to the extraction of glueball masses from these correlation functions and discuss first the case of the negative parity 2^- state excited by the tensor T_a. As Fig. 22 shows, a sufficiently large fiducial volume exists for extracting masses for the two ensembles and the two values agree within 5% with an average of 8.3. We will come back to this state when discussing products of three field-strength operators.

Similarly, the analysis of the correlation function of T_+ already discussed above (cf. Fig. 19) yields for the same ensembles a common slope of about 8. The discussion of the Wilson loop correlation function will provide additional information on the corresponding 2^+ state.

Also in the T_- correlation function, 2^+ states appear as intermediate states. As the left side of
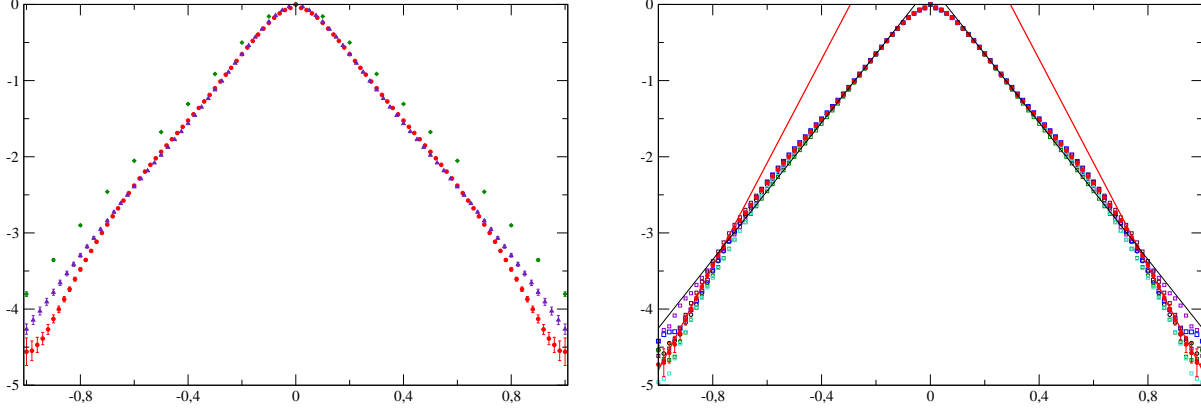

Figure 24: Left: Correlation function of T_- for different ensembles $(N_I, \rho) = (50, 0.16)$ - green, $(50, 0.08)$ - red, $(50, \text{variable } \rho)$ - indigo. Right: Correlation function of T_- (red) and components for the ensemble $(50, 0.08)$. The values of the slopes are 4.5 and 6.8.

Fig. 24 shows, this correlation function is rather exceptional, in that the fiducial intervals for the different ensembles extend to distances of up to 1. A fit to these correlation functions for $|t| \leq 0.6$, the fiducial interval also used for the other correlation functions, yields an average value of 4.1 for the slope. At larger values of $|t|$, the slopes of the correlation functions for the different ensembles start to deviate. As is seen from the right side of this figure, the correlation function for the $(50, 0.08)$ ensemble displays an increase in slope by a factor 1.5. Furthermore, as the decomposition in different components indicates, this change of slope is not accompanied by a significant violation of rotational invariance. A change to a larger slope also occurs though more moderately around $t = 0.6$ in the $(50, 0.16)$ (from 3.7 to 4.9) and in the $(50, \text{variable } \rho)$ (from 4.1 to 5.2) ensembles. For determination of a glueball mass, we have to use the larger values of the slope as more realistic. The change to a larger slope with increasing separation suggests that for this particular operator, the regime in which the time evolution is governed by a transfer matrix has not been reached in the region $|t| \leq 0.6$ where the smaller slopes are extracted. As for the T_+ - T_a relation, our numerical results for the momentum projected correlation functions of $\mathbf{P}$ and T_- agree for $|t| \leq .4$ within 6%, indicating that, like the correlation function of the integrated Poynting vector, the correlation function of the integrated T_- operator has no interpretation in terms of glueballs in this regime. Despite their rather complicated structure, the correlation functions of T_- exhibit the expected scaling behavior as shown in Fig. 20. However the strong dependence of the larger slope on the instanton size (4.9 - 6.8) prevents extraction of a glueball mass from this correlation function. Given the comparatively small fiducial interval $(0.7 \leq |t| \leq 1)$, we cannot rule out that several states contribute with weights depending on the instanton size. In this case we can only deduce an upper limit for the mass

$$m_{2^+} \leq 4.9 \,. \tag{119}$$

T_3

We turn now to a discussion of correlation functions associated with observables composed of

products of 3 field-strength operators. We will study excitations of $1^\pm$ states and reexamine the excitation of $2^\pm$ states. Since the field-strengths are evaluated at the same point, very rapid variations in the vicinity of the center of the pseudoparticles result.
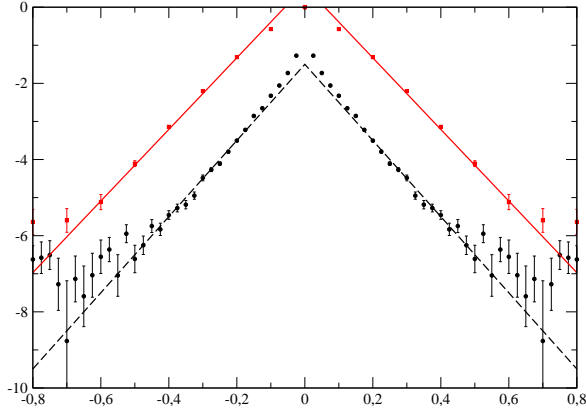

Figure 25: T_3 correlation function for the ensemble of 50 instantons of variable size (black circles) and 800 instantons ($L = 4$) of size $\rho = 0.16$ (red squares), the value of the slopes is -9.3.

Due to these rapid variations significant results could not be obtained for the $0^\pm$ excitations which contain single instanton contributions. In the case of the $1^\pm$ and $2^\pm$ excitations, where single pseudoparticles do not contribute, the variations due to the interference with the "mean field" are still too large for generating reliable results for the smallest instanton size ($\rho = 0.04$) considered. Consequently the fiducial intervals are in general significantly smaller than in the case of products of two field-strength components. The correlation function of the 2^- operator T_3 shown in Fig. 25 displays at small $|t|$ rapid variations and a strong dependence on the individual ensembles. In particular, the ensemble with variable ρ exhibits for small $|t|$ an almost singular behavior. Beyond this region, a sufficiently large fiducial interval exists where a common slope can be extracted for the two ensembles. The value of 9.3 differs by 10% from the value 8.3 in Fig. 22. The average of these two values will be used subsequently. A meaningful extraction of a slope parameter of the correlation functions for the 2^+ operator $(\mathbf{E} \times \mathbf{E}) \otimes \mathbf{B}$ was not possible and is not discussed here.

V_a, V_p
We finally turn to a discussion of the spin 1 correlation function in Fig. 26. For both, the V_a and V_p [cf. Eq. (102)] correlation functions, the three ensembles exhibit, beyond the small $|t|$ region, sufficiently large fiducial intervals for extracting the slopes reliably. The average values of these slopes are used later.

W_r^{00}, W_r^{2m}
For various ensembles, we have investigated Wilson loop correlation functions for loops of different radii. We have considered both Wilson loops of fixed radius and homogeneously distributed radii. For an appropriate choice of the parameters, the observables have been found to be insensitive to this choice. Due to the higher computational complexity as compared to the correlation functions of the local operators, less configurations and for a given configuration
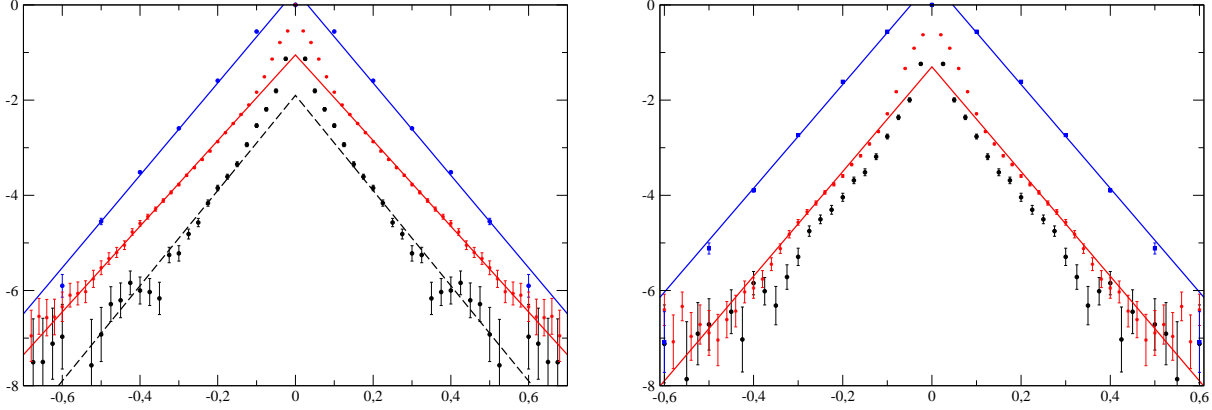
Figure 26: Axial V_a (left) and polar vector V_p (right) correlation functions for ensembles of 50 instantons of variables size (black circles), of size $\rho = 0.16$ (blues squares) and $\rho = 0.08$ (red stars). The values of the slopes are $-9.0, -9.7, -10.0$ (V_a) and $-10.5, -11.0$ (V_p).

fewer points for the momentum projection had to be used. The use of Wilson loop correlation functions did not improve the determination of the 0^+ glueball mass, since also in this case difficulties due to the subtraction of the vacuum expectation value with the concomitant sensitivity to deficits in rotational and translational invariance occur. As shown by the right side of Fig. 27, slopes (or masses) could be extracted from the 2^+ correlation functions with an average value of about 8 and an uncertainty of about 15%. Form this figure we also can read off the relative normalization of the correlation functions for the different sizes of the Wilson loops. As compared to the correlation functions for $\langle r \rangle = 0.2$ the strength of the coupling to the 2^+ excitations is enhanced by a factor of 5.7 for the correlation function with $\langle r \rangle = 0.4$. One therefore might expect a larger systematic uncertainty in the slope extracted for $\langle r \rangle = 0.2$. As the figure shows, the size of the Wilson loop that produces the maximal overlap with the exited 2^+ state is 0.4 and the extracted slope essentially does not change when varying the size from 0.3 to 0.4. Adopting the rational that the maximal overlap produces the most meaningful slope, we extract from this correlation function the value 7.7. We observe that this result is within $\sim 10\%$ compatible with the slope extracted from the T_+ correlation function. We also note that the fact that the overlap is maximal for a Wilson loop of radius $r = 0.4$ implies that the size of the state is approximately 0.47 fm, consistent with lattice calculations [29, 30].

5.3 The Glueball Spectrum

The results for the glueball masses extracted from our investigations of correlation functions of local operators built from 2 and 3 field-strength operators and from the non-local Wilson loop operators are summarized in Table 6. After a rescaling, our results are compared in Fig. 28 to the results of the lattice gauge calculation of Ref. [31]. In comparison with the lattice results, the energy scale is too small by roughly a factor of 2. For a more detailed comparison we have rescaled our results with a factor of 2.2, which makes the value of the average excitation energy
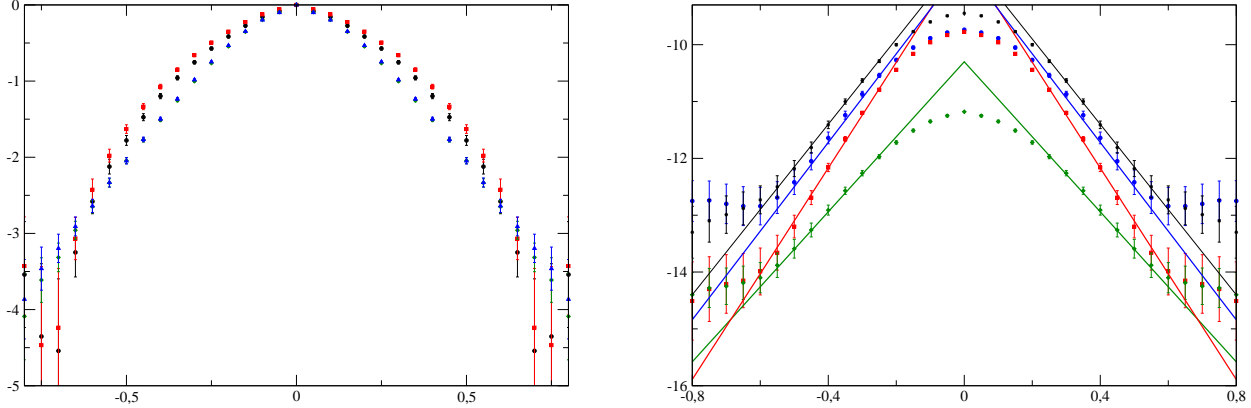
Figure 27: Left: Wilson loop correlation functions $D_\ell(t)$ (111) for $\ell = 0$ (red squares), $\ell = 2$ (blue triangles), $N = 50, \rho = 0.16$ and $\langle r \rangle = 0.1$ compared with field-strength correlators of $\mathbf{B}^2$ (black circles) and $\mathbf{B} \otimes \mathbf{B}$ (green diamonds). The two $\ell = 2$ correlation functions are virtually indistinguishable. Right: Wilson loop correlation functions $D_2(t)$ (111) for $N = 50, \rho = 0.08$ and $\langle r \rangle = 0.2, 0.3, 0.4, 0.5$ (green diamonds, blue circles, blacks stars, red squares). The extracted slopes are $-6.6, -7.8, -7.5, -9.3$.

state	slope	slope/$\sqrt{\sigma}$
0^+	4.0	1.6
2^+	7.7	3.1
2^-	8.8	3.5
1^+	9.6	3.9
1^-	10.8	4.4

Table 6: Glueball masses. Note that errors are discussed in the text and are not indicated here.

agree for the two spectra. Having adjusted the overall scale, we note that the masses of the 0^+, 2^- and $1^\pm$ glueballs of the two spectra agree within 5% while the mass of the 2^+ state is 25% larger than the lattice value. We find this agreement surprising also in view of the large adjustment of the overall scale. These final results do not account for the possible existence of a second 2^+ with an upper limit (after rescaling) for the mass of [cf. Eq. (119)]

$$m_{2^+} \leq 2\sqrt{\sigma}.$$

As emphasized above, the smallness of the fiducial intervals did not permit us to firmly establish or rule out the existence of an additional low mass 2^+ state.

The correlation functions for meron ensembles yield a very similar spectrum although the uncertainties in the extraction of the slopes, for the reasons discussed above, are significantly higher. In particular, finer details like the splitting of the $1^\pm$ states could not be determined. As for the instanton ensembles, the existence of a 2^+ state, essentially degenerate with the 0^+ excitation, cannot be ruled out. The overall scale factor necessary to reproduce the average excitation energy of the lattice results is 1.8.
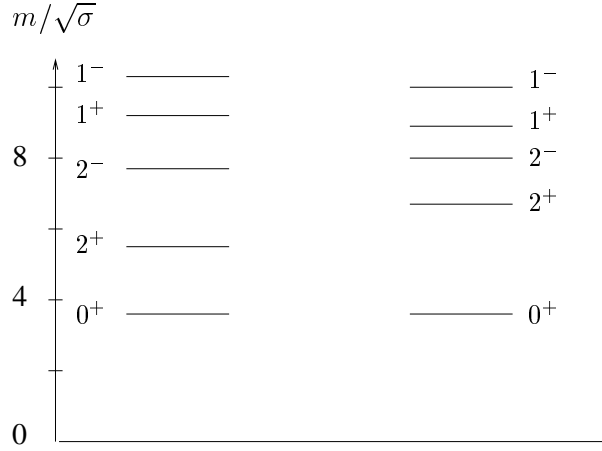
Figure 28: Spectra of $0^+, 2^\pm, 1^\pm$ glueball states of SU(2) Yang-Mills Theory. Left: Lattice gauge theory [31]. Right: Masses from pseudoparticle ensembles after rescaling (see text).

5.4 Wilson Loop Correlation Functions and Confinement

In this concluding paragraph of our studies of correlation functions, we will return to the issue of confinement in the pseudoparticle ensembles. The physics of confinement is intimately related to the formation of flux-tubes or gauge strings and one may wonder whether the area law found in the fit to the Wilson loops indeed implies that such a mechanism is operative also in the pseudoparticle ensembles. To study the dynamics of Wilson loops we follow the investigations in [32] and calculate correlation function of loops with fixed orientation. We assume circular loops of equal radius which are parallel to each other and orthogonal to the direction of separation. We do not perform any averaging, i.e., we calculate the following correlators [cf. Eq. (108)]

$$C_r(t) = \langle W_r(\mathbf{n}, \mathbf{x}_0, t) W_r(\mathbf{n}, \mathbf{x}_0, 0) \rangle \,. \tag{120}$$

The results of the calculations are shown in Fig. 29. If one assumes that the application of the Wilson loop operator to the vacuum generates a gauge string with (approximate) energy

$$E = 2\pi\sigma r \,,$$

the relevant variable for describing the correlation function is rt. As Fig. 29 shows, the three correlation functions are described approximatively by a universal curve in terms of this variable. It thus appears that the dynamics in the pseudoparticle ensembles is compatible with the formation of gauge strings or flux tubes. The existence of such a universal curve offers the possibility for an alternative determination of the string tension. Due to the limited range of values a direct extraction of the string tension is not possible. We have parameterized the distributions by

$$\ln W = -\frac{a(rt)^2}{\sqrt{b + a(rt)^2}} \,. \tag{121}$$

From the fit to the correlation functions of the Wilson loops shown in the right part of Fig. 29 we obtain

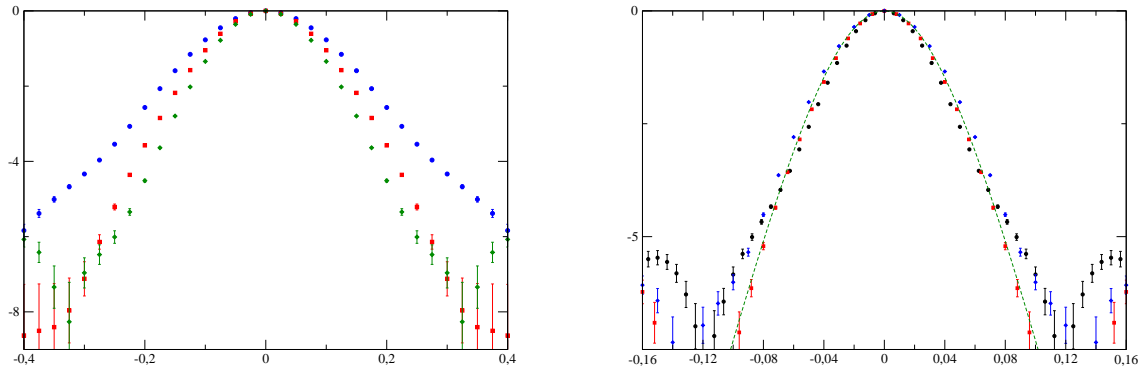$$\sigma = \frac{\sqrt{a}}{2\pi} = 17.4 \pm 6. \tag{122}$$

48

Figure 29: Left: Logarithm of correlation functions of circular Wilson loops with fixed parallel spatial orientation for an ensemble of 500 instantons of size $\rho = 0.08$ as a function of separation in time t for 3 values of the Wilson loop radius $r = 0.25$ (black circles), $r = 0.32$ (red squares), $r = 0.40$ (blue diamonds) . Right: The same as a function of the variable rt.

The small range of relevant values of the variable rt does not permit a more precise determination of σ. The value (122) of the string tension agrees within 20% with that derived from the asymptotics of the Wilson loops (cf. Eqs. (75) and (76)).

At large separations the universality breaks down as expected. For $rt \geq r^2$ it becomes energetically favorable for the system of two loops to couple by annihilation of the gauge string to the vacuum or glueball states. This corresponds to the Gross-Ooguri phase transition in the large N_c limit [33].

6 Conclusions

The effective theories with pseudoparticle degrees of freedom studied in this work describe important properties of QCD. The regular gauge instantons or the merons with their long-range gauge fields apparently constitute a proper and economical set of degrees of freedom in the description of the Yang-Mills dynamics in the infrared. By superposition of these building blocks, field configurations are generated with confinement as an inherent property. An area law for sufficiently large Wilson loops is already obtained in (stochastic) ensembles with the same weight assigned to all field configurations. However such ensembles violate basic principles. The action of field configurations in such ensembles is diverging in the infrared, concomitantly the ensembles do not possess a proper thermodynamic limit and violate translational invariance. By assigning the standard weight given by the action to the field configurations, all these problems are cured at once and confinement is preserved. The resulting configurations not only confine static color charges but also the building blocks themselves. Only at the expense of a logarithmically diverging action can a building block be removed to infinity. The pseudoparticles are strongly correlated over large distances in order to prevent a logarithmic rise in the action (for this reason a global update procedure had to be employed in our computations). On the other

49

hand with its many spikes and valleys in color singlet quantities like the action density or the topological susceptibility, single field configurations appear strongly disordered.

Thus, in our investigations, a picture of the Yang-Mills vacuum emerges which is that of a nematic substance – a medium that is strongly correlated in color or "director" space (S^3 and $\mathbb{R}P^2$ respectively) and which at the same time is essentially disordered in configuration space (cf. [34]). This picture summarizes our findings. On the one hand, updates of the randomly chosen coordinates of the pseudoparticles in addition to the color update have no significant effect. On the other hand, a color disordered ensemble such as the stochastic ensemble we have studied does not produce a qualitatively correct model of the Yang-Mills vacuum. Clearly, the color correlations in meron and instanton ensembles are at the heart of the phenomenon of confinement. When a singular gauge instanton contributes to 2 Polyakov lines, it produces a linear potential, while singular instantons affecting one Polyakov line only are irrelevant. The last part of this argument [5] gets modified in our context. Due to the strong color correlations, single instantons still contribute to the potential. In addition to confinement of static charges, the color correlated fields reproduce remarkably well other important features of the Yang-Mills dynamics. They exhibit proper scaling under variations of the number of pseudoparticles or the size of the system and they reproduce qualitatively characteristic properties such as the values of the gluon condensate and the topological susceptibility. Unlike the gluon condensate, the value of the topological susceptibility can be related to the single pseudoparticle properties. We also have been able to investigate finer details and for instance to show analytically that characteristic properties of the Wilson loops in the limits of small and large size, i.e., the U(1) and the string limit, are qualitatively reproduced. Here the role of the pseudoparticle size as an effective ultraviolet regulator is essential. We also qualitatively confirmed the string picture for Wilson loop correlation functions and thus obtained a significant consistency check of the description of confinement in term of pseudoparticles.

The outcome of our investigations of correlation functions is more ambiguous. We have demonstrated the emergence of a hadronic scale under the usual circumstances where the size of the building blocks is smaller than the emerging size of the "many-body" hadron. In the case of merons with their long range field-strength the opposite mechanism is at work and establishes a hadronic size smaller than the constituent meron size. To study hadronic excitations, we have computed momentum projected correlators of local gauge invariant operators with definite angular momentum built from field-strength bilinears and trilinears and have also calculated correlation functions of momentum and angular momentum projected Wilson loops. With these computations, we have been able to determine the spectrum of glueballs with quantum numbers $0^+, 1^\pm$ and $2^\pm$. While the structure of the spectrum agrees qualitatively with the corresponding lattice results, the masses determined are too small by an overall factor of about 2 for both instanton and meron ensembles. We have not been able to uniquely identify the origin of this difficulty. Ambiguities in the determination of the string constant are unlikely to explain it. A smaller value deduced from the fit to the Wilson loop would, after identification with the empirical value, result in a higher energy scale. There is indeed some freedom left by redefinition of the relevant interval of the area of the loops. A change of the order of 20% cannot be ruled out entailing a 10% change in the energy scale. Corrections of a similar order of magnitude seem to result when using a "smeared" Wilson loop [35]. Neither effect however approaches the necessary factor of 4 in the string tension. The most likely explanation is that with the pseudoparticle ensembles primarily determined by infrared properties, the ultraviolet fluctuations

are not adequately described. For a description of an object like the scalar glueball with a size of approximately 0.2 fm [29] the spatial resolution of our field configurations – possibly limited by a too "small" number of pseudoparticles – may just be insufficient. In our discussion of small size Wilson loops we indeed have noticed the disappearance of the "Coulomb regime" with the disappearance of the disorder in color space. To cure this problem one would have to either significantly enlarge the number of pseudoparticles or to introduce additional degrees of freedom which improve the description of the vacuum at small scales. Candidates for such additional degrees of freedom are singular gauge instantons which are the center reflected partners of the regular gauge instantons. Inclusion of these degrees of freedom would, by construction, avoid the otherwise problematic issue of multiple counting of gauge copies.

In addition to such improvements in the description of the Yang-Mills theory, for phenomenological applications quarks have to be incorporated. Here the advantages of the continuum formulation of the effective pseudoparticle theories could be essential. First steps in this endeavor have been taken [36]. Here one aims to take over the successful treatment of the dynamics of quarks in the instanton liquid model [8]. The ultimate goal would be to establish in this way an effective theory that exhibits the two nonperturbative basic phenomena of QCD – confinement and chiral symmetry breaking.

Acknowledgements

References

[1] A. A. Belavin, A. M. Polyakov, A. S. Schwartz and Yu. S. Tyupkin, Phys. Lett. B **59** (1975), 85.

[2] C. G. Callan, R. F. Dashen, D. J. Gross, F. Wilczek and A. Zee, Phys. Rev. D **18** (1978), 4684.

[3] V. de Alfaro, S. Fubini and G. Furlan, Phys. Lett. B **65** (1976), 163.

[4] C. G. Callan, R. F. Dashen and D. J. Gross, Phys. Rev. D **19** (1979), 1826 .

[5] C. G. Callan, R. F. Dashen and D. J. Gross, Phys. Rev. D **17** (1978), 2717 .

[6] C. G. Callan, R. F. Dashen and D. J. Gross, Phys. Lett. B **66** (1977), 375.

[7] E. V. Shuryak, Nucl. Phys. B **203** (1982), 93.

[8] T. Schafer and E. V. Shuryak, Rev. Mod. Phys. **70** (1998), 323, [arXiv:hep-ph/**9610451**].

[9] D. Diakonov and V. Y. Petrov, Nucl. Phys. B **245** (1984), 259.

[10] D. Diakonov and V. Y. Petrov, Nucl. Phys. B **272** (1986), 457.

[11] F. Lenz, J. W. Negele, M. Thies, Phys. Rev. D **69** (2004), 074009, [arXiv:hep-th/**0306105**].

[12] M. Wagner, Phys. Rev. D **75** (2007), 016004, [arXiv:hep-ph/**0608090**].

[13] A. M. Brzoska, F. Lenz, J. W. Negele, M. Thies, Phys. Rev. D **71** (2005), 034008, [arXiv:hep-th/**0412003**].

[14] M. Campostrini, A. Di Giacomo and G. Paffuti, Z. Phys. C **22** (1984), 143.

[15] M. A.Shifman, A. I. Vainshtein and V. I. Zakharov, Nucl. Phys. B **147** (1979), 385, 448.

[16] S. Narison, Phys. Lett. B **387** (1996), 162, [arXiv:hep-ph/**9512348**].

[17] E. Witten, Nucl. Phys. B **156**, 269 (1979).

[18] G. Veneziano, Nucl. Phys. B **159**, 213 (1979).

[19] B. Lucini and M. Teper, JHEP **0106** (2001), 050, [arXiv:hep-lat/**0103027**].

[20] M. Lüscher and P. Weisz, JHEP **0207** (2002), 049, [arXiv:hep-lat/**0207003**].

[21] J. Ambjørn, P. Olesen and C. Peterson, Nucl. Phys. B **240** (1984), 189.

[22] K. Dietz and T. Filk, Phys. Rev. D **27** (1983), 2944.

[23] G.S. Bali, Phys. Rev. D **62** (2000), 114503, [arXiv:hep-lat/**0006022**].

[24] P. de Forcrand and O. Philipsen, Phys. Lett. B **475** (2000), 280, [arXiv:hep-lat/**9912050**].

[25] K. Kallio and H. Trottier Phys. Rev. D **66** (2002), 034503, [arXiv:hep-lat/**0001020**].

[26] S. Kratochvila and P. de Forcrand, Nucl. Phys. B **671** (2003), 103, [arXiv:hep-lat/**0306011**].

[27] E. Vicari, Nucl. Phys. B **554**, 301 (1999), [arXiv:hep-lat/**9901008**].

[28] Y. Chen, A. Alexandru, S. J. Dong, T. Draper, I. Horvath, F. X. Lee, K. F. Liu, N. Mathur, C. Morningstar, M. Peardon, S. Tamhankar, B. L. Young, J. B. Zhang, Phys. Rev. D **73**, (2006), 014516, [arXiv:hep-lat/**0510074**].

[29] P. de Forcrand and K.-F. Liu, Phys. Rev. Lett. **69** (1992), 248, [arXiv:hep-lat/**9211054**].

[30] M. Loan and Y. Ying, [arXiv:hep-lat/**0603030**].

[31] M. J. Teper, [arXiv:hep-ph/**9812187**].

[32] F. Lenz, "Dynamics of Wilson Loops in QCD" in "Continuous Advances in QCD 2006", World Scientific (2007); A. M. Brzoska, F. Lenz, and D. Steinbacher, to be published.

[33] D. J. Gross, H. Ooguri, Phys.Rev. D **58** (1998),106002, [arXiv:hep-th/**9805129**].

[34] F. Lenz, "Topological Concepts in Gauge Theory", in "Topology and Geometry in Physics", Lecture Notes in Physics, Springer Berlin (2005), [arXiv:hep-th/**0403286**].

[35] C. Szasz and M. Wagner, to be published.

[36] C. Szasz, Diploma Thesis, University of Erlangen (2006).